Journal of Neuroinflammation

RESEARCH

Open Access

Spatiotemporal dynamic changes of meningeal microenvironment influence meningeal lymphatic function following subarachnoid hemorrhage: from inflammatory response to tissue remodeling

Bingrui Zhu[1,2,3†], Changming Liu[4†], Ming Luo[5†], Jiarui Chen[1,2,3], Sixuan Tian[1,2,3], Tiantong Zhan[1,2,3], Yibo Liu[1,2,3], Haocheng Zhang[1,2,3], Zhen Wang[1,2,3], Jianmin Zhang[1,2,3], Yuanjian Fang[1,2,3*], Sheng Chen[1,2,3*] and Xiaoyu Wang[1,2,3*]

Abstract

Background Meningeal lymphatic vessels (mLVs) play a critical role in clearing erythrocytes from the subarachnoid space and immune cells from the brain parenchyma following subarachnoid hemorrhage (SAH). However, the drainage function of mLVs is impaired during the acute stage after SAH and gradually recovers in the subacute phase. We aimed to investigate the meningeal transcriptional response post-SAH and elucidate the dynamic influence of meningeal microenvironment on meningeal lymphatic function.

Methods We employed bioinformatics analysis of single-cell RNA sequencing and spatial transcriptomics to characterize the spatiotemporal dynamic changes in the early meningeal microenvironment post-SAH. In a mouse model of SAH, the early dynamic changes of the meningeal immune cells and the potential growth factor that promoted the early repair of the mLVs were further investigated and validated.

Results During the acute phase, myeloid cells early infiltrated the meninges and triggered inflammatory responses. In the subacute phase, the fibroblast population expanded significantly, contributing to tissue remodeling. The interplay between immune cells and fibroblasts regulated cell migration and phenotypic transition, potentially affecting the function of mLVs. Notably, placental growth factor (PGF) emerged as the most prominent ligand within the VEGF

†Bingrui Zhu, Changming Liu and Ming Luo contributed equally to this work.

*Correspondence:
Yuanjian Fang
sandman0506@zju.edu.cn
Sheng Chen
saintchan@zju.edu.cn
Xiaoyu Wang
wxy95@zju.edu.cn
Full list of author information is available at the end of the article

© The Author(s) 2025. **Open Access** This article is licensed under a Creative Commons Attribution-NonCommercial-NoDerivatives 4.0 International License, which permits any non-commercial use, sharing, distribution and reproduction in any medium or format, as long as you give appropriate credit to the original author(s) and the source, provide a link to the Creative Commons licence, and indicate if you modified the licensed material. You do not have permission under this licence to share adapted material derived from this article or parts of it. The images or other third party material in this article are included in the article's Creative Commons licence, unless indicated otherwise in a credit line to the material. If material is not included in the article's Creative Commons licence and your intended use is not permitted by statutory regulation or exceeds the permitted use, you will need to obtain permission directly from the copyright holder. To view a copy of this licence, visit http://creativecommons.org/licenses/by-nc-nd/4.0/.

signaling pathway received by meningeal lymphatic endothelial cells (mLECs) post-SAH. This signaling event was associated with the early recovery of mLVs after acute immune responses.

Conclusions Our study revealed a spatiotemporal transformation of the meningeal microenvironment from an "inflammatory response" phase to a "tissue remodeling" phase following SAH. Monocyte-derived macrophages and self-recruiting neutrophils contributed to impairment of mLVs in the acute stage, while PGF might serve as a key factor promoting early meningeal lymphatic function repair following the inflammatory response. These findings provided novel insights into the cellular dynamics underlying mLVs dysfunction and recovery post-SAH.

Keywords Subarachnoid hemorrhage, Meningeal lymphatic function, Meningeal microenvironment, Immune-fibroblast crosstalk, Single-cell RNA sequencing, Spatial transcriptomics

Graphical Abstract

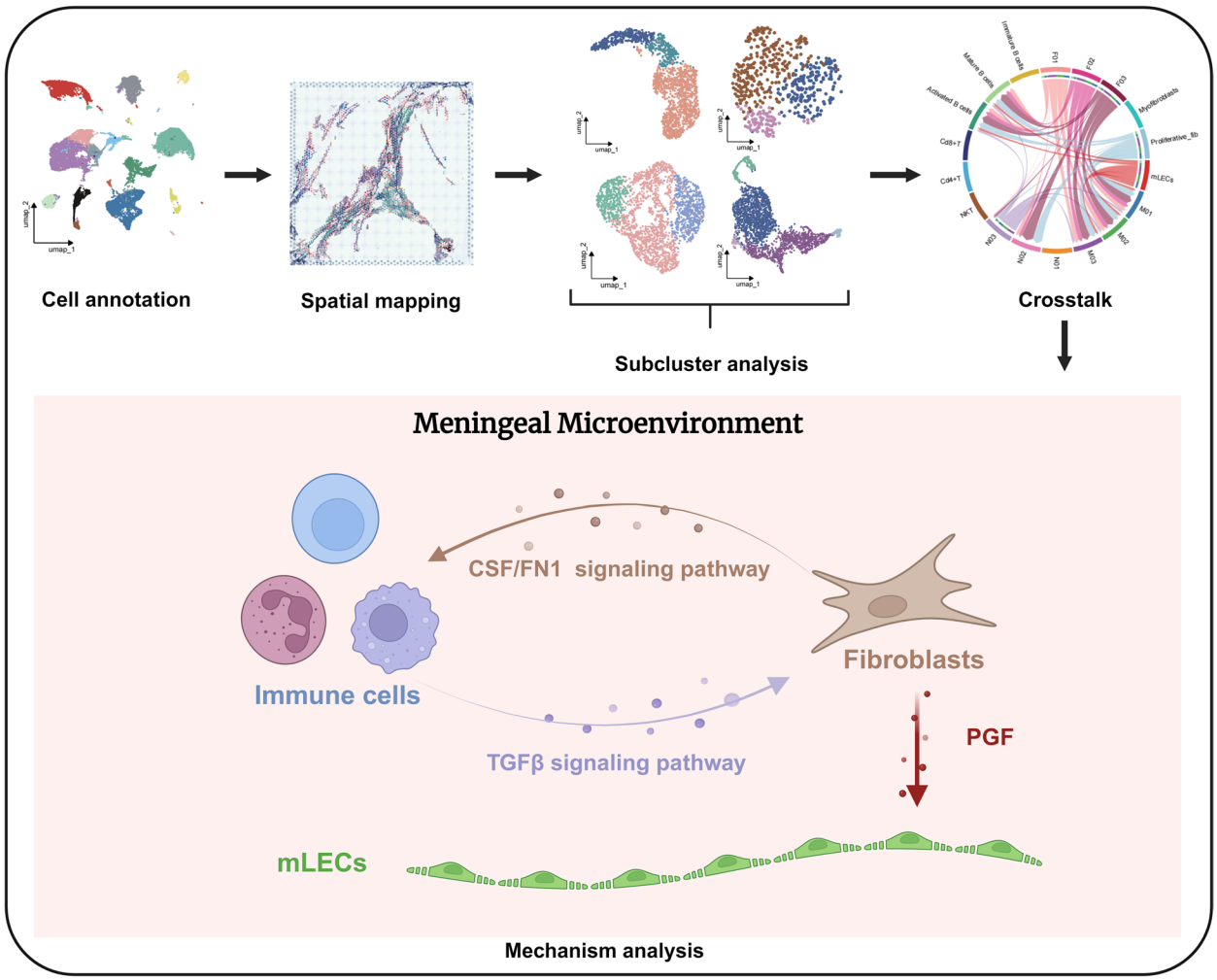

Introduction

The meninges serve as a crucial peripheral barrier of the central nervous system (CNS), providing structural support while accommodating diverse immune cells and fibroblasts [1]. The discovery of meningeal lymphatic vessels (mLVs) within the dura mater has significantly expanded our understanding of CNS immune regulation and metabolic waste clearance [1]. Beyond waste removal, mLVs actively participate in immune surveillance, and their function is closely

regulated by meningeal immune cells [2]. Additionally, immune-fibroblast crosstalk plays a role in shaping the inflammatory response, tissue remodeling, and fibrosis within the meninges [3, 4].

The dysfunction of mLVs has been implicated in multiple CNS disorders. In neurodegenerative diseases such as Alzheimer's disease and Parkinson's disease, impaired meningeal lymphatic drainage exacerbates pathological protein deposition, neuroinflammation, and neuronal damage. Conversely, enhancing the meningeal lymphatic function alleviates these pathological manifestations [5, 6]. In acute CNS injuries, such as traumatic brain injury and stroke, mLVs contribute to the regulation of brain-peripheral immune crosstalk, neuroinflammation, and tissue repair [7–9]. Notably, in hemorrhagic stroke conditions like intracerebral hemorrhage (ICH) and subarachnoid hemorrhage (SAH), mLVs facilitate the clearance of extravasated blood and immune cells, influencing disease progression [9–11].

SAH is a severe type of hemorrhagic stroke characterized by high mortality and disability rates [12, 13]. The extravasation of blood into the subarachnoid space triggers a cascade of inflammatory and oxidative stress responses, exacerbating secondary brain injury post-SAH [11, 14, 15]. Clinical evidence has indicated that accelerating blood clearance from the cerebrospinal fluid can improve neurological recovery in SAH patients [16, 17]. The mLVs have been reported to play a key role in clearing erythrocytes from the subarachnoid space and draining immune cells from the cerebral parenchyma post-SAH [10, 11]. However, impaired drainage function of mLVs worsens cerebral ischemia and edema, further aggravating brain damage [2, 18, 19]. Our previous study demonstrated that the meningeal lymphatic function exhibited dynamic changes in a mouse model of SAH, with the most severe drainage dysfunction observed at 24 h (24 h) post-SAH, followed by partial recovery at 72 h (72 h) [2].

Despite these insights, the precise influential mechanism underlying the dynamic transitions of meningeal cell subtypes and immune-fibroblast interaction on meningeal lymphatic function following SAH remains unclear. To address this gap, we employed single-cell RNA sequencing (scRNA-seq) and spatial transcriptomics (ST-seq) to comprehensively characterize the spatiotemporal dynamics of the meningeal microenvironment following SAH, with a particular focus on the interaction between immune cells and fibroblasts in modulating meningeal lymphatic function.

Methods

Experimental design

The study consisted of four parts, as illustrated in Fig. 1 and Table S1.

1. Bioinformatics analysis: The single-cell RNA sequencing (scRNA-seq) and spatial transcriptome sequencing (ST-seq) datasets from Sham, SAH 24 h and 72 h mouse meningeal samples were accessed from previous research conducted by Wang et al. [2]. To investigate the pathophysiological mechanisms underlying spatiotemporal dynamic changes of meningeal microenvironment following SAH, we conducted a secondary analysis of scRNA-seq (Sham group, SAH 24 h group, SAH 72 h group, 10 mice per group) and ST-seq (Sham group, SAH 24 h group, SAH 72 h group, 1 mouse per group) data of mice from our previous study [2]. The primary bioinformatics analysis methods included: basic analysis of scRNA-seq data, gene set enrichment analysis (GSEA), gene ontology (GO) enrichment analysis, pseudotime analysis, cell–cell interaction analysis, robust cell type decomposition (RCTD).
2. Experiment 1: A total of 23 mice were used in this experiment, and 3 of these mice died. To validate the composition of the meningeal immune microenvironment following SAH, we induced SAH in mice (SAH 24 h group, SAH 72 h group, 10 mice per group). The intact meninges were collected from the skullcap of the mice for flow cytometry analysis to assess changes in meningeal immune cell following SAH.
3. Experiment 2: A total of 29 mice were used in this experiment, and 3 of the mice died. We performed immunofluorescence to representatively show the characteristics of bilateral hotspots of mLVs in the acute phase of SAH (Sham group, SAH 24 h group, 1 mouse per group). Furthermore, we conducted immunofluorescence to explore whether acute PGF treatment could enhance the drainage function of the meningeal lymphatic system following SAH (Sham group, SAH 24 h + Vehicle group, SAH 24 h + VEGF-C group, SAH 24 h + PGF group, 4 mice per group). Additionally, we performed immunofluorescence to ascertain whether PGF blocking could inhibit the recovery of mLVs post-SAH (SAH 72 h + IgG group, SAH 72 h + AntiPGF group, 4 mice per group).
4. Experiment 3: A total of 65 mice were used in this experiment, and 5 of the mice died. We used the modified garcia scale, pole test and wire hanging test to assess the effects of acute PGF treatment (Sham group, SAH 24 h + Vehicle group, SAH 24 h + VEGF-C group, SAH 24 h + PGF group, 10 mice per group)

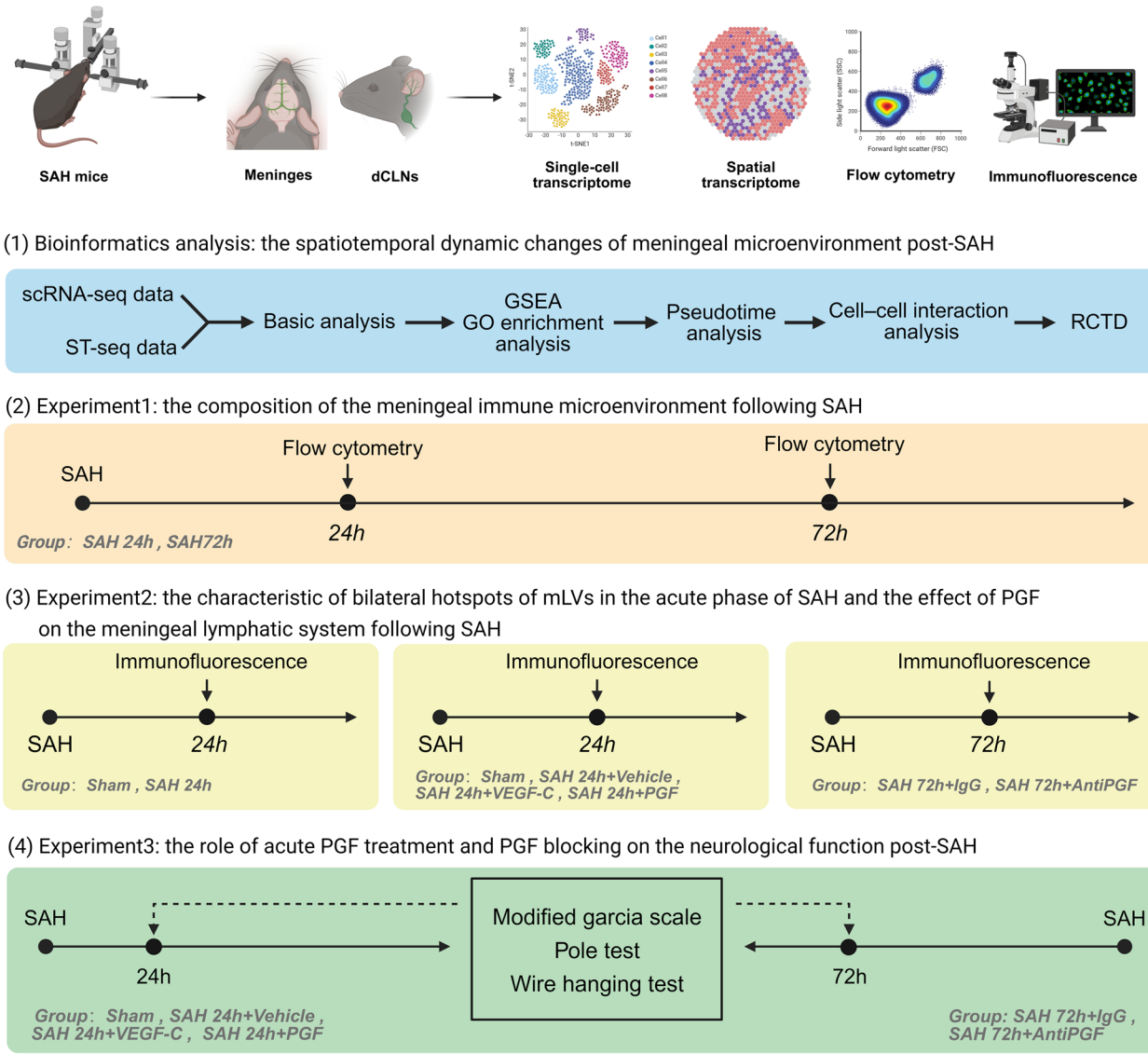

Fig. 1 The framework of this experiment

and PGF blocking (SAH 72 h + IgG group, SAH 72 h + AntiPGF group, 10 mice per group) on the neurological function.

Animals

Young male C57BL/6 mice (8–10 weeks old, 23–25 g, total of 117 mice) were purchased from Shanghai SLAC Laboratory Animal Company Limited. Mice were housed in animal facilities with controlled habituation and temperature, on a 12/12-h light/dark cycle. Food and water were provided ad libitum. Mice were allowed to accommodate for 2 weeks before experiments. All animal experiment protocols were approved by the Institutional Ethics Committee of the Second Affiliated Hospital, Zhejiang University School of Medicine (approval No. 2024–220). All procedures involving mice strictly followed the guidelines of the National Institutes of Health for the care and use of laboratory animals.

SAH model

Subarachnoid hemorrhage (SAH) was induced by prechiasmatic cistern blood injection, as described previously [20]. Briefly, after anesthesia with 1% pentobarbital via intraperitoneal injection, the head was fixed in a stereotactic device and then the skull was exposed along the midline. A small hole was drilled 4.5 mm anterior to the bregma. Using a Hamilton syringe (100μL, 26-gauge

needle), 60μL of autologous blood was extracted from the tail artery of the mouse, and the needle angled horizontally at a 40° angle and inserted through the hole to contact the skull base. The blood was slowly injected within 10 s through the needle. After 5 min, the needle was slowly removed to avoid backflow. To prevent the pain of surgery, ketoprofen (5 mg/kg) was used as an analgesic in animals received surgery. Mice were treated with ketoprofen 30 min before surgery and for 1–2 day (once/day) after operation via subcutaneous injection. The treatment duration was adapted to the tissue collection schedule. The same procedure was conducted on mice without blood injection to serve as the sham group. For antibody injection: we performed antibody injection to inhibit PGF in the meninges post-SAH to ascertain whether blockade of PGF protein in vivo would affect the outcomes, following a published protocol from previous experiments [2]. We injected a mixture of the blocking antibody with autologous blood into the prechiasmatic cisternae. Administering the anti-PGF antibody at the same site and time as the blood injection ensured immediate and localized neutralization of PGF during the initiation of SAH-induced acute inflammation and meningeal lymphatic impairment. A mixture of 10 μg/mL PGF antibody (R&D Systems, MAB264) or isotype IgG control (R&D Systems, MAB002) with 60 μL autologous blood was injected into the prechiasmatic cisternae. The needle was left in place for 5 min after injection to avoid backflow.

Intra-Cisterna Magna (ICM) Injections

The anesthesia and perioperative analgesia methods were the same as above. The head was fixed in the stereotaxic apparatus. The head holder was adjusted to lower the nose and tilt the head downward at approximately 30 degrees relative to the horizontal plane. This positioning effectively elevated the neck, thereby facilitating exposure of the cisterna magna. The neck skin was disinfected, then, the skin was incised along the midline of the neck, and the muscle tissue was separated to expose the cisterna magna area. Using a Hamilton syringe (coupled to a 33-gauge needle), the volume of the desired solution was injected into the cisterna magna compartment. For the fluorescent tracer experiments: 2μL of fluorescent beads (Thermo Fisher Scientific, yellow-green fluorescent 505/515, F8813) were drawn and injected into the cisterna magna at a rate of 0.2μL/min, as described previously [2, 21]. The procedure was performed 2 h before animal euthanasia. Additionally, the fluorescent tracer should be protected from light during experiments. For the recombinant protein experiments: we performed recombinant protein treatment to determine whether the PGF protein influenced early outcomes and possessed early therapeutic potential. We attempted intrathecal injection treatment at an early stage (1 h) post-SAH. Recombinant proteins were injected into the cisterna magna 1-h post-SAH to enable therapeutic delivery after the initial hemorrhagic event occurred, which simulated a clinical therapeutic intervention. The administration protocol and dosage were referenced from previous studies [11, 16, 22]. 1 μg of recombinant proteins VEGF-C (MedChemExpress, HY-P74474) and PGF (SinoBiological, 50,125-MCCH) were diluted in 2μL of sterile PBS respectively. Intra-Cisterna Magna injections were performed using a Hamilton syringe (5μL, 33-gauge needle) at a rate of 0.2μL/min. This procedure was performed 1 h after SAH in the animals. The needle was retracted 2 min after injection to prevent backflow.

Immunofluorescence and image quantification of deep cervical lymph nodes (dCLNs) or meninges

Mice were euthanized with lethal doses of pentobarbital-based euthanasia agent. The dCLNs were collected under the microscope and fixed in 4% paraformaldehyde (PFA) for 2 h at 4 °C. Then the dCLN clearance was performed following the CUBIC clearance protocol, and simultaneously stained the dCLNs with DAPI (1:1000) during the clearance. Mice were transcardially perfused with 0.1 M phosphate-buffered saline (PBS) and 4% PFA, then the intact skullcap was removed and fixed in 4% PFA for 24 h at 4 °C. After dehydration in 15% and 30% sucrose solutions, the meninges were carefully dissected from the skullcaps. The meninges were blocked with 2% donkey serum or 2% goat serum, 1% bovine serum albumin, 0.1% triton, 0.05% tween-20, and 0.05% sodium azide in PBS for 2 h at room temperature and then incubated at 4 °C overnight with the following primary antibodies or DAPI (1:500): Rabbit anti-Lyve1 (Cell Signaling Technology, 67,538, 1:100), Goat anti-Cd31 (R&D Systems, AF3628, 1:100), Rat anti-Ly6g+ Ly6c (Abcam, ab25377, 1:100). The meninges were then washed three times for 10 min at room temperature in PBS and 0.05% tween-20, followed by incubation with Donkey Alexa Fluor 594 anti-Goat (Thermo Fisher Scientific, A11058, 1:500), Donkey Alexa Fluor 647 anti-Rabbit (Thermo Fisher Scientific, A31573, 1:500), Donkey Alexa Fluor 594 anti-Rabbit (Thermo Fisher Scientific, A21207, 1:500) and Donkey Alexa Fluor 488 anti-Rat (Thermo Fisher Scientific, A21208, 1:500) for 2 h at room temperature in the same solution used for blocking. The meninges were washed three times for 10 min at room temperature in PBS and then spread out on glass slides with mounting medium and coverslips. The dCLNs and meninges processed in the above manner were imaged respectively using a Leica DMI8 confocal microscope and LAS X software (Leica Microsystems).

Quantitative analysis of the images was conducted using Imaris and ImageJ software. The results of lymph nodes were analyzed by Imaris software. The percentage of the volume occupied by beads in the lymph nodes after three-dimensional reconstruction was calculated to evaluate the drainage function of meningeal lymphatic system. The results of meninges were analyzed by ImageJ software. The vascular density was measured by using the VesselJ tool. To evaluate the proportion of the $Lyve1^+$ area, we calculated the $Lyve1^+/CD31^+$ vascular density ratio. Given the regional aggregation of beads within mLVs, calculating the area alone does not provide an accurate measurement of bead distribution. Therefore, the mean fluorescence intensity of beads across the coverage area of mLVs was measured to assess the drainage function of the meningeal lymphatic system.

Flow cytometry

Mice were euthanized with lethal doses of pentobarbital-based euthanasia agent and transcardially perfused with 20 ml of cold 1× PBS. Heads were removed and skullcaps were dissected and harvested using small surgical scissors and put directly in ice-cold Dulbecco's Modified Eagle Medium (DMEM). Subsequently, dura maters were carefully removed from interior aspect of the skulls under a microscope. Due to the small amount of dura mater tissue, two dura mater samples from mice in the same group would be combined into one sample for flow cytometry. Following this, dura maters were immersed in 1 mL DMEM with 60 U/mL DNase 1 and 0.6 U/mL collagenase blend. The resulting mixture underwent enzymatic digestion at 37 °C for a duration of 25 min. Cell suspensions were then stirred and put into a single tube after filtration through a 70-μm nylon mesh cell strainer. Cells were centrifuged at 400 g at 4 °C for 10 min. The supernatant was removed and the dura mater cells were resuspended with ice-cold 1× PBS. Cells were stained for extracellular marker with immune cell associated antibodies to anti-CD45-Pacific Blue (BD Biosciences, CYT-45PBZ-R, 1:200), anti-CD3e-FITC (BD Biosciences, 553,062, 1:200), anti-NK-1.1-BV605 (BD Biosciences, 564,143, 1:200), anti-Ly6G-PerCP-Cy5.5 (BD Biosciences, 560,602, 1:200), anti-CD11b-PE-Cy7 (BD Biosciences, 552,850, 1:200), anti-CD19- PE (BD Biosciences, 557,399, 1:200) and anti-CD11c-BV711 (BD Biosciences, 563,048, 1:200). Incubation with antibodies lasted 30 min at 4 °C and was followed by centrifugation at 400 g at 4 °C for 10 min and a 1 ×PBS wash. Cells were finally suspended in 500 μL of 1× PBS and analyzed using a FACScan flow cytometer. Data processing was finished with FlowJo and Excel. Statistical analysis was performed using GraphPad Prism.

Assessment of neurological function for mice

The Modified Garcia scale (0–18 points) included six subtests: response capacity, alertness, coordination, motor skills, complex movements, and balance [23]. A blinded investigator conducted the neurological assessments at 24 h and 72 h after SAH. A higher score indicated better neurological function.

For the pole test [23], mice were trained three times daily for 3 days before the start of testing and then a pole test was performed 24 h and 72 h post-SAH. Animals were placed on top of a 50–55 cm vertical pole with a diameter of 8–10 mm and trained to turn around and descend the pole. Scoring commenced upon the initiation of the animal's turning movement. The time taken to complete a full 180° turn (T_{turn}) and the latency to reach the ground (T_{total}) were meticulously documented. If a mouse failed to execute a turn and descended laterally, T_{total} was equated to $T_{turn.}$ If a mouse completed a turn, descended halfway, and eventually fell, the recorded time stopped when it reached the ground. The maximum time of 60 s was imposed for the test.

The Wire Hanging test evaluated grip strength, balance, and endurance in mice [2]. Mice were trained to suspend their body by holding on to a single wire stretched between two posts 50–60 cm above the ground, with their hind limbs taped to restrict the usage of all four paws. A pillow was placed between the two posts to avoid injury in case of falls."Latency to fall"served as the primary endpoint for evaluating motor performance, with a maximum testing time of 60 s. Mice were trained three times daily for 3 days before the start of testing.

The neurological function assessment was performed by a blinded investigator.

Basic analysis of scRNA-seq data

The scRNA-seq data was preprocessed by CellRanger. The filtered data was further analyzed in R (v4.3.3) with the Seurat R package (v5.1.0) [24]. Briefly, cells were included with detected genes ranging from 350 to 5500 and a mitochondrial gene ratio of less than 10%. Data normalization and variance stabilization were carried out with the SCTransform method. Principal component analysis (PCA) was used to reduce the dimensionality. The FindClusters function was applied to identify different clusters. The uniform manifold approximation and projection (UMAP) was used to visualize the cell distribution. Differentially expressed genes (DEGs) were identified using the Wilcoxon rank-sum test implemented in the FindAllMarkers function. Only genes with adjusted $p \leq 0.05$ and $\log_2$(fold change) > 0.25 or < -0.25 were considered DEGs. Cell clusters were annotated to known cell lineages using well recognized marker genes from

CellMarker 2.0 database (http://bio-bigdata.hrbmu.edu.cn/CellMarker or http://117.50.127.228/CellMarker/) [25] and PanglaoDB database (https://panglaodb.se/) [26].

Gene set enrichment analysis

Gene set enrichment analyses (GSEA) were performed with clusterProfiler R package (v4.10.1) [27]. For each comparison group, all genes identified by FindMarkers in Seurat (v5.1.0) (with thresholds set as min.pct = 0.1 and logfc.threshold = 0) were ranked by their average $\log_2$ fold change (avg_log2 FC). FDR q-values were used to determine statistical significance. We conducted GSEA to identify the Kyoto Encyclopedia of Genes and Genomes (KEGG) pathways that were induced or repressed in meninges 24 and 72 h post-SAH.

Gene ontology enrichment analysis

Gene Ontology (GO) enrichment analyses were performed with clusterProfiler R package (v4.10.1) [27]. The GO reference gene sets were acquired from MSigDB databases (https://www.gsea-msigdb.org/gsea/msigdb/) [28].

Pseudotime analysis

The Monocle (v2.30.0) R package [29] was used for pseudo-time analysis. We reduced the dimension with the DDRTree algorithm. The cellular trajectory was performed with the orderCells function and the plot_cell_trajectory function.

Cell–cell interaction analysis

The CellChat R package (v1.6.1) [30] was used to infer intercellular communication between meningeal lymphatic endothelial cells (mLECs) and main meningeal cell subcluster. Briefly, normalized expression values of mLECs and main meningeal cell subcluster were run in the R tool. The identifyOverExpressedGenes, identifyOverExpressedInteractions and projectData functions were applied to perform preprocessing. The probability of interactions within each cluster was calculated with computeCommunProb, computeCommunProbPathway, aggregateNet and netAnalysis_computeCentrality functions. Finally, the netAnalysis_signalingRole_heatmap function was applied to identify the senders and receivers in the network.

Spatial deconvolution of ST-seq with scRNA-seq reference

The raw ST-seq data was preprocessed using Space Ranger. Seurat (v5.1.0) was used to process Space Ranger output data files [24]. We used SCTransform to normalize the data, ScaleData to standardize the data, RunPCA for dimensionality reduction, FindNeighbors and FindClusters to cluster the spatial transcriptome points, and RunUMAP for data visualization. AddModuleScore function was used to calculate a module of a biological process. Robust Cell Type Decomposition (RCTD) was performed for spatial deconvolution to connect scRNA-seq data.

Statistical analysis

All statistical analysis methods were described in the figure legends. All data are presented as mean ± standard deviation (SD). Normality was assessed using the Shapiro–Wilk test. To compare the statistical significance between the two groups, the Student's t-test or the Mann–Whitney test (both two-tailed) was performed. One-way analysis of variance (ANOVA) followed by Tukey's multiple comparisons test or Kruskal–Wallis test followed by Dunn's multiple comparison test were used to detect differences between groups. All statistical analyses were performed with GraphPad Prism (v.9.5.1) and $p < 0.05$ was considered to identify statistical significance.

Results

Overview of early spatiotemporal transcription profiling of meninges after SAH

To deeply understand the spatiotemporal changes in the meningeal microenvironment after SAH, we analyzed the data of scRNA-seq and ST-seq of meninges from SAH mouse models at 24 h and 72 h post-SAH. After initial quality control and removal of doublets, we obtained single-cell transcription data for 22,721 cells (8,731 from the Sham group, 7,296 from SAH 24 h group, 6,694 from SAH 72 h group). Based on typical markers from the CellMarker 2.0 and PanglaoDB databases, we identified 16 cell types, including macrophages, monocytes, neutrophils, dendritic cells, mast cells, T cells, B cells, NK cells, fibroblasts, endothelial cells, smooth muscle cells, schwann cells, choroid plexus cells, erythroid-like and erythroid precursor cells, neurons, proliferating cells (Fig. 2A-D; Table S2). Some cluster markers were referenced from Wang et al. [2]. In the Sham group, non-immune cells were dominant in the meninges. Among them, fibroblasts and endothelial cells were the main types. At 24 h, the meningeal immune response was activated, and myeloid cells, including mainly monocytes-macrophages and neutrophils, became dominant in the meninges. At 72 h, the meningeal immune response weakened compared to 24 h. The level of neutrophils decreased, while the number of fibroblasts increased sharply, becoming the most abundant cell type (Fig. 2C). The GSEA results illustrated that the pro-inflammatory pathways such as the "TNF signaling pathway", "NF − κB signaling pathway" and "Neutrophil extracellular trap formation" were significantly activated at SAH 24 h. At

72 h, these pro-inflammatory pathways were downregulated compared to 24 h (Fig. 2E). Flow cytometry further revealed changes in the composition of the meningeal immune microenvironment after SAH (Fig. 2F-H; Fig. S1). In the $CD45^{high}$ population, the percentage of myeloid cells was approximately five times that of lymphocytes at 24 h post-SAH. At 72 h, the myeloid-to-lymphoid ratio was about 2 (Fig. 2F). At 24 h, neutrophils and mono-macrophages were the major components of myeloid cells. By 72 h, neutrophils had a significant decrease (Fig. 2G). The proportion of lymphocytes was small at 24 h, while there was a notable increase in T cells at 72 h (Fig. 2H). ST-seq further revealed the dynamic changes of cell types in the mLVs area. Fibroblasts and endothelial cells were spatially located around mLVs under homeostasis. Activated monocytes and neutrophils significantly infiltrated the mLVs at 24 h, while macrophages became the prominent cell type around mLVs at 72 h (Fig. 2I). Our previous research has shown that the drainage function of mLVs was most severely impaired at SAH 24 h. The drainage function of mLVs began to gradually recover by 72 h [2]. To further investigate the influence of the meningeal microenvironment on the meningeal lymphatic system, we conducted subpopulation analysis of the major immune cells and meningeal fibroblasts within the meninges.

Early dynamic changes of macrophage subtypes infiltrating around mLVs post-SAH

Our results indicated that macrophages were one of the main immune cell types in the meningeal microenvironment during different phases post-SAH (Fig. 2C, G). Therefore, macrophages may play a key role in the immune response within the meningeal microenvironment. We performed subcluster analysis of macrophages and identified three main subclusters (M01-M03) (Fig. 3A, B).

M01 primarily overexpressed monocyte-related genes (*Chil3, Ly6c2*) and early macrophage recruitment genes (*Ccr2*). M01 might originate from monocytes infiltrating meningeal tissue from blood in the acute phase. Monocytes predominantly reside in the blood within the venous sinuses. They can migrate to meningeal tissue under the influence of cytokines or inflammatory factors and differentiate into macrophages. Additionally, M01 differentially expressed *Spp1*. Antigen presentation-related MHC II encoding genes (*H2-Eb1, H2-Ab1, H2-Aa, Cd74*) were highly expressed in M02. M03 mainly expressed genes related to phagocytosis receptors (*Mrc1, Cd163*) (Fig. 3C; Table S3).

In the sham group, the meningeal tissue-resident macrophages only included M02 and M03, and their levels were almost equal. At 24 h post-SAH, the number of M01 subcluster increased significantly and it became the dominant subtype. At 72 h, M02 became the main subcluster of macrophages (Fig. 3D). Among them, GO enrichment analysis revealed that different macrophage subtypes might participate in different biological processes. M01 might be involved in the "regulation of inflammatory response" and "acute inflammatory response". M02 was mainly involved in "antigen processing and presentation of peptide antigen via MHC class II" and "positive regulation of T cell activation". The biological function of M03 was related to "positive regulation of protein kinase activity", "response to transforming growth factor beta", and "regulation of cellular response to growth factor stimulus"(Fig. 3E). To understand the association among macrophage subgroups, we performed trajectory analyses. Pseudotime analysis indicated a differentiation trajectory from M01 to M03 along M02 (Fig. 3F). ST-seq data clearly showed the spatial distribution of macrophage subtypes around mLVs across the groups. Under steady-state, the predominant macrophage subcluster around the venous sinuses and mLVs was M03. M01 heavily infiltrated around the area at 24 h, with the highest enrichment in the bilateral hotspots of the mLVs. At 72 h, M02 became the major subgroup of macrophages distributing around the venous sinuses and mLVs (Fig. 3G).

(See figure on next page.)

Fig. 2 Single-cell profiling of the meningeal microenvironment after SAH. **A**, **B** UMAP projection of cells in the meninges colored by manually annotated clusters (**A**) and samples (**B**). **C** Stacked bar plot showing the proportion of cell clusters in each group. **D** Dot plot illustrating the expression levels of cell typing genes in each cluster using Wang et al. as a reference [2]. **E** KEGG enrichment analyses of ranked gene lists from three different sample groups based on GSEA. **F** Flow cytometric analysis of myeloid-to-lymphocyte ratio of CD45 high cells in the SAH 24 h and SAH 72 h group **G** Flow cytometric analysis of neutrophil and mono-macrophage percentage of CD45 high cells in the SAH 24 h and SAH 72 h group. **H** Flow cytometric analysis of T, NK and B cell percentage of CD45 high cells in the SAH 24 h and SAH 72 h group. (n = 10, the dura mater from two mice in the same group were combined into one sample for flow cytometry; unpaired two-tailed Mann–Whitney test for B cell percentage, unpaired two-tailed Student's t-test for others). All data was represented as mean ± SD. *$p < 0.05$, **$p < 0.01$, ns represents no statistical difference. **I** The spatial spot map corresponding to the annotations of single-cell sequence, with different colored spots representing different clusters

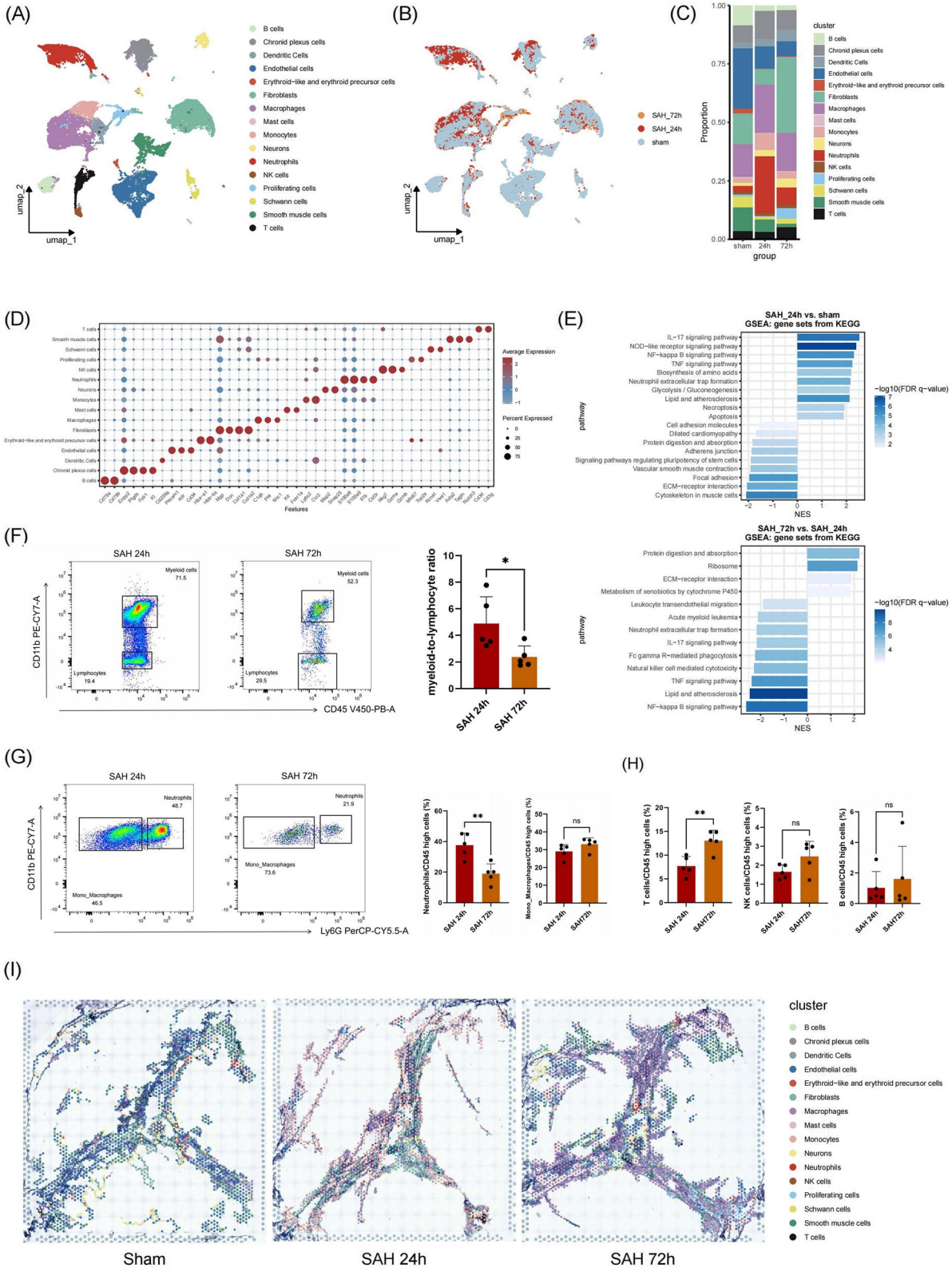

Fig. 2 (See legend on previous page.)

Neutrophils induced the strong self-recruitment within 24 h post-SAH to promote meningeal immune response

Under the steady-state, the proportion of tissue-resident neutrophils in the meninges is particularly low. A large number of neutrophils infiltrated the meninges during the acute phases following SAH. Neutrophils became one of the main types of immune cells, and then decreased in later stages (Fig. 2A-C, G).

Analysis of neutrophil subtypes revealed three distinct subpopulations in the meninges after SAH (Fig. 4A). Among them, N01 and N02 were predominant in sham and SAH 72 h groups (Fig. 4B, D). N01 mainly expressed the naïve stage associated genes (*Ngp, Camp, Chil3*) and dominated in the sham and SAH 72 h group. N02 highly expressed chemotaxis related genes (*Ccl6, Cxcr2*) (Fig. 4C; Table S4). At SAH 24 h, N03 became the main subcluster, constituting 89% of all neutrophils (Fig. 4D). N03, the predominant subgroup of neutrophils at 24 h post-SAH, highly expressed chemotaxis-related genes (*Cxcl2, Ccl3, Ccl4*) and pro-inflammatory genes (*Tnf, Il-1β*) (Fig. 4C, E; Table S4). N03 activated the inflammatory response in the meningeal microenvironment in the acute phase. On one hand, N03 released inflammatory factors (such as TNF and IL-1β), promoted the inflammatory response in the meninges as well as exerted potential neurotoxic effects (Fig. 4E). On the other hand, it also produced pro-inflammatory chemokines, and the CXCL and CCL signaling pathways were the main pathways for promoting the chemotaxis of myeloid cells. Interestingly, we found a self-chemotaxis phenomenon within neutrophils in the acute inflammatory stage. N03 was self-recruited through the CXCL2-CXCR2 signaling pathway (Fig. S2A-C). This ligand-receptor pair has been reported as a common self-chemotaxis pathway for neutrophils [31, 32]. Our pseudotime analysis revealed that N01 was in the naïve stage, N03 was the most mature subcluster, and N02 was in an intermediate developmental stage between N01 and N03 (Fig. 4F). ST-seq analysis showed the spatial distribution of different neutrophil subtypes around the venous sinuses and mLVs at different stages. In the acute phases, both N02 and N03 mainly infiltrated around the venous sinuses and mLVs. Additionally, N02 and N03 were mainly distributed in the hotspots of mLVs (Fig. 4G). Immunofluorescence confirmed that neutrophils infiltrated the bilateral hotspots of mLVs at 24 h (Fig. 4H).

Effects of SAH on the meningeal lymphocyte transcriptome

Studies have reported that meningeal lymphocytes, including T and B cells, may play a crucial role in potentially influencing the drainage function of mLVs, regulating cerebral homeostasis and neurological function [33–35]. Flow cytometry revealed that T cells dominated the lymphocyte population at both 24 h and 72 h following SAH, while the number of B cells was relatively sparse (Fig. 2H; Fig. S1). At 72 h post-SAH, the proportion of T cells among immune cells began to increase (Fig. 2H). We conducted subgroup analyses of T and B cells to investigate the subtype changes and interactions between meningeal T and B cells after SAH. According to classical markers [32], T cells are classified into three typical subgroups: $Cd4^+$ T, $Cd8^+$ T, and NKT (Fig. 5A-C; Table S5). Based on the maturation markers of B cells [36], B cells are divided into three subclusters, including Immature B cells, Mature B cells, and Activated B cells (Fig. 5D-F; Table S6). Mature B cells express high levels of the B cell maturation marker *Cd37* and the genes of the B cell receptor (*Cd79a, Cd79b*). Activated B cells specifically and highly expressed genes related to MHC II molecules (*H2-Aa, H2-Eb1, H2-Ab1*). Immature B cells primarily expressed *Rag1* and *Il7r* (Fig. 5F). Additionally, we analyzed the differentiation trajectory of B cells, indicating that Immature B cells have the lowest maturity level, while Activated B cells have the highest. Mature B cells fall in between these two subclusters (Fig. 5G). GO enrichment analysis revealed that the function of Immature B cells and Mature B cells was mainly associated with immune development and lymphocyte activation. The Activated B cells with the highest differentiation degree could process and present antigen to activate $Cd4^+$ T cells (Fig. 5H). Cell–cell interaction analysis further revealed that $Cd4^+$ T cells received signaling from MHC II-related ligand-receptor pairs at 72 h post-SAH (Fig. 5I). Activated B cells and the M02 subgroup of macrophages, as antigen-presenting cells (APCs), interact with Cd4 receptors through MHC II molecules, contributing to the activation of $Cd4^+$ T cells.

(See figure on next page.)

Fig. 3 The dynamic change of meningeal macrophage subtypes post-SAH. **A**, **B** UMAP projection of meningeal macrophage subpopulations colored by clusters (**A**) and samples (**B**). **C** Dot plot illustrating marker genes for the three macrophage subclusters. **D** Stacked bar plot demonstrating the proportion of meningeal macrophage subclusters in each group. **E** GO enrichment analyses of DEGs among the three macrophage subtypes. **F** Developmental trajectories of meningeal macrophage subclusters. **G** Predicted spatial localization of meningeal macrophage subtypes around mLVs by RCTD

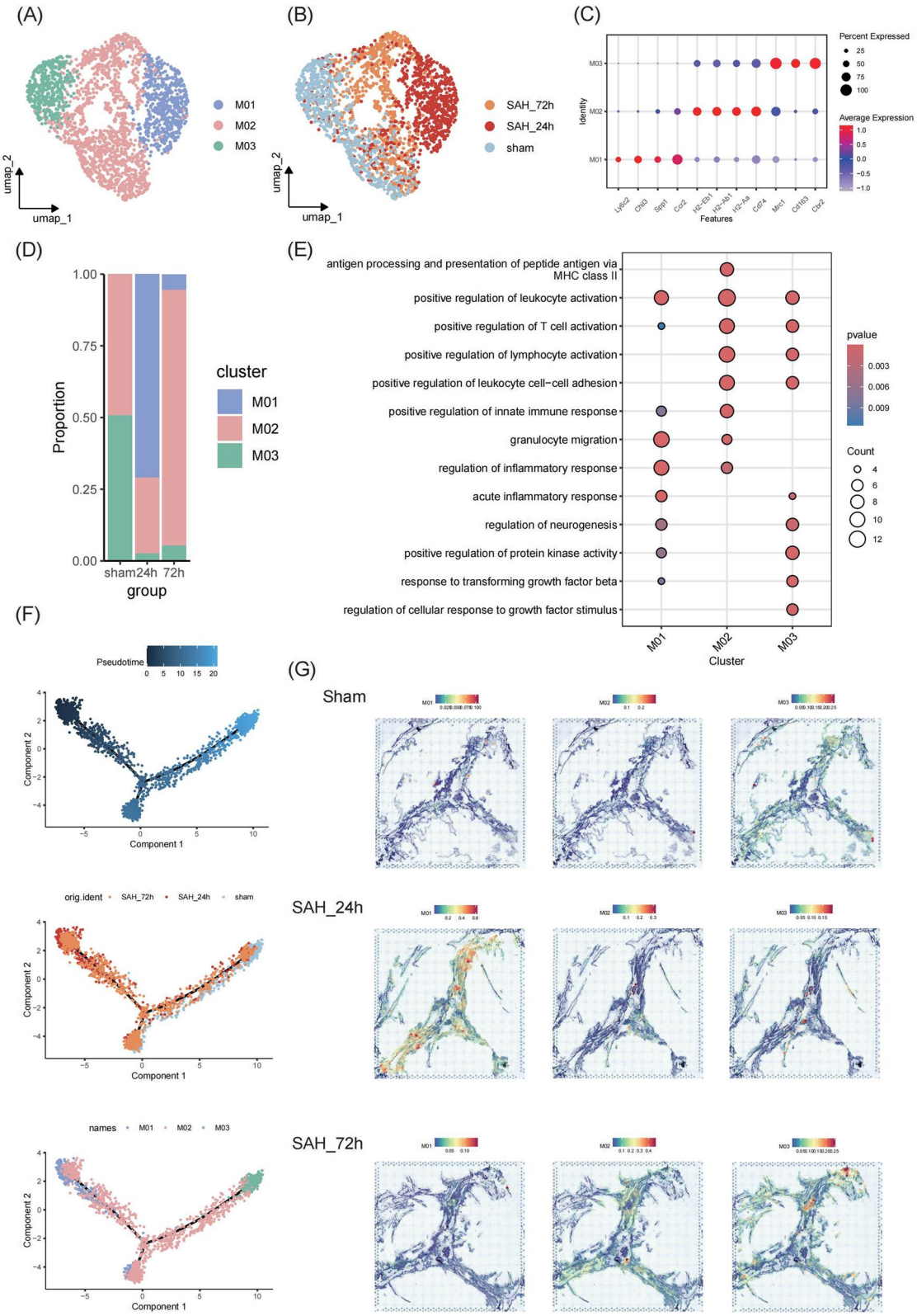

Fig. 3 (See legend on previous page.)

Transcriptional modulation of meningeal fibroblasts following SAH

Our previous experiment illustrated that the drainage function of mLVs was gradually improved at SAH 72 h [2]. Meanwhile, the proportion of meningeal fibroblasts significantly increased, becoming one of the most abundant cell types in the meningeal microenvironment (Fig. 2C). We further analyzed the subpopulation changes and spatial distribution of fibroblasts to explore the association between fibroblasts and the repair of mLVs.

We conducted subgroup analysis of meningeal fibroblasts and identified five subtypes with different highly expressed genes, including F01 (*Pgf, Smoc1, Nov*), F02 (*Apod, Apoe, Tgfbr2*), F03 (*Zbp1, Ifit1, Ifit2, Ifit3*), myofibroblasts (*Acta2, Tagln, Postn*), and proliferative fibroblasts (*Pgf, Mki67, Top2a, Stmn1*) (Fig. 6A; Fig. S3A-C; Table S7). GO enrichment analysis further revealed potential functions of various subtypes. F01 might be associated with angiogenesis, wound healing, and negative regulation of leukocyte activation and adhesion. F02 and myofibroblasts were primarily responsible for maintaining the extracellular matrix (ECM) structure and the growth and development of smooth muscle and connective tissue. F03 was related to immune response regulation. Proliferative fibroblasts were mainly associated with the cell cycle (Fig. 6B). F02 was the predominant resident subtype under homeostasis. F01 and proliferative fibroblasts were activated and began to increase significantly after SAH. F01 became the most prevalent subtype at 72 h post-SAH (Fig. 6C). Pseudotime analysis revealed that the developmental trajectory of meningeal fibroblasts progressed from proliferative fibroblasts at the naïve stage through F01, F03, and F02 to myofibroblasts (Fig. 6D). ST-seq analysis illustrated prominent collagen production around mLVs at 72 h post-SAH, compared to the sham and SAH 24 h groups (Fig. 6E). Additionally, we further revealed the distribution characteristics of fibroblast subtypes around mLVs. F02 and myofibroblasts were the two subtypes with the densest distribution around mLVs particularly in Sham group. Their distribution characteristics corresponded to the potential biological function in maintaining the normal ECM structure around mLVs. Furthermore, F01 and proliferative fibroblasts surrounding mLVs gradually increased following SAH. At 72 h post-SAH, F01 and proliferative fibroblasts around mLVs gathered at the hotspot regions (Fig. 6F).

The crosstalk of immune cells and fibroblasts post-SAH

To further reveal the complexity of the meningeal microenvironment, we utilized CellChat to construct the interaction network between immune cells and fibroblasts in the meninges following SAH.

The CCL and CXCL signaling pathways were dominant at immune cell chemotaxis following SAH (Fig. S4). Neutrophils and macrophages were the most active participants. Among them, N02 and N03 released the most chemotactic signals at both 24 h and 72 h, primarily contributing to the self-recruitment among neutrophil subpopulations. M01 and M02 released higher levels of chemotactic signals at 24 h. At 72 h, however, M03 significantly enhanced its chemotactic effect to recruit T cells through the CXCL signaling pathway (Fig. S4).

There were some signaling pathways in the crosstalk between immune cells and fibroblasts, mainly including CSF (CSF1-CSF1R), TGFβ (TGFβ1-TGFβR1/2, TGFβ1-ACVR1/TGFβR1), FN1 (FN1-SDC4, FN1-CD44, FN1-ITGα4/ITGβ1) (Fig. 7A, B; Fig. S5A-D; Fig. S6A-D). Fibroblasts regulated macrophage phenotype via CSF1-CSF1R signal (Fig. S5B; Fig. S6B). Fibroblasts primarily received TGFβ signals from macrophages (Fig. S5C; Fig. S6C). Additionally, fibroblasts could secrete FN1 to interact with the majority of immune cell subpopulations (Fig. S5D; Fig. S6D).

PGF treatment improves the meningeal lymphatic drainage function and neurological outcomes in mice after SAH

VEGF-C has been demonstrated to be the most significant factor in the proliferation and development of mLECs, which can enhance the meningeal lymphatic drainage function [37]. To investigate the association between meningeal lymphatic repair and VEGF signaling, we profiled the VEGF signaling network within the meningeal microenvironment at 72 h post-SAH (Fig. 8A). The PGF-VEGFR1 ligand-receptor pair represents the most significant interaction in the VEGF signaling pathway received by mLECs (Fig. 8B). Fibroblasts, especially

(See figure on next page.)

Fig. 4 Self-recruited neutrophils enhance meningeal inflammatory response within 24 h following SAH. **A**, **B** UMAP projection of meningeal neutrophil subtypes colored by clusters (**A**) and samples (**B**). **C** Dot plot illustrating marker genes for the neutrophil subclusters. **D** Stacked bar plot showing the proportion of meningeal neutrophil subtypes in each group. **E** Feature plot depicting several significantly upregulated pro-inflammatory genes in N03. **F** Developmental trajectories of meningeal neutrophil subclusters. **G** Predicted spatial localization of meningeal neutrophil subpopulations around mLVs by RCTD. **H** Representative image of the bilateral hotspots area on mLVs in Sham and SAH 24 h group

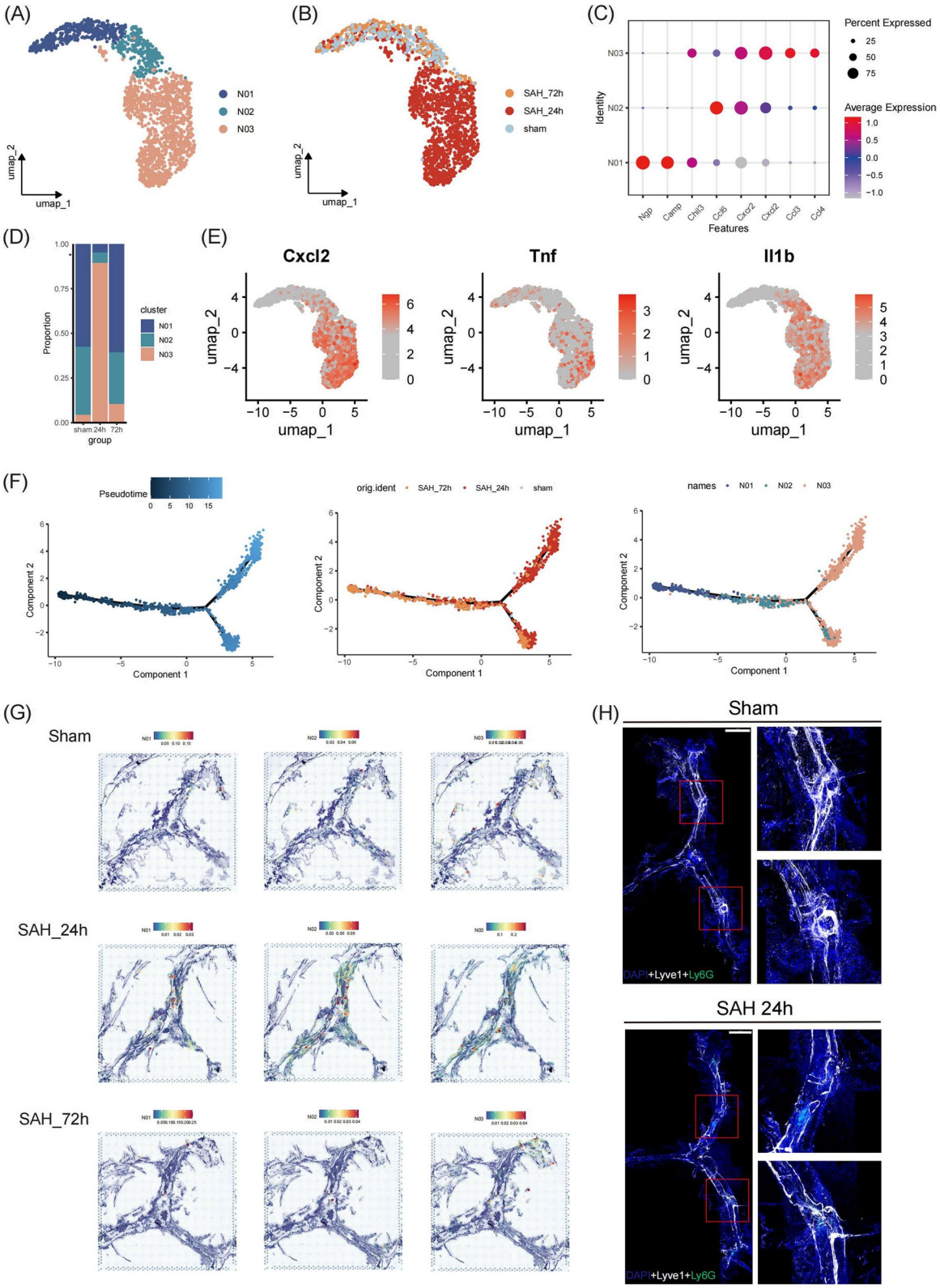

Fig. 4 (See legend on previous page.)

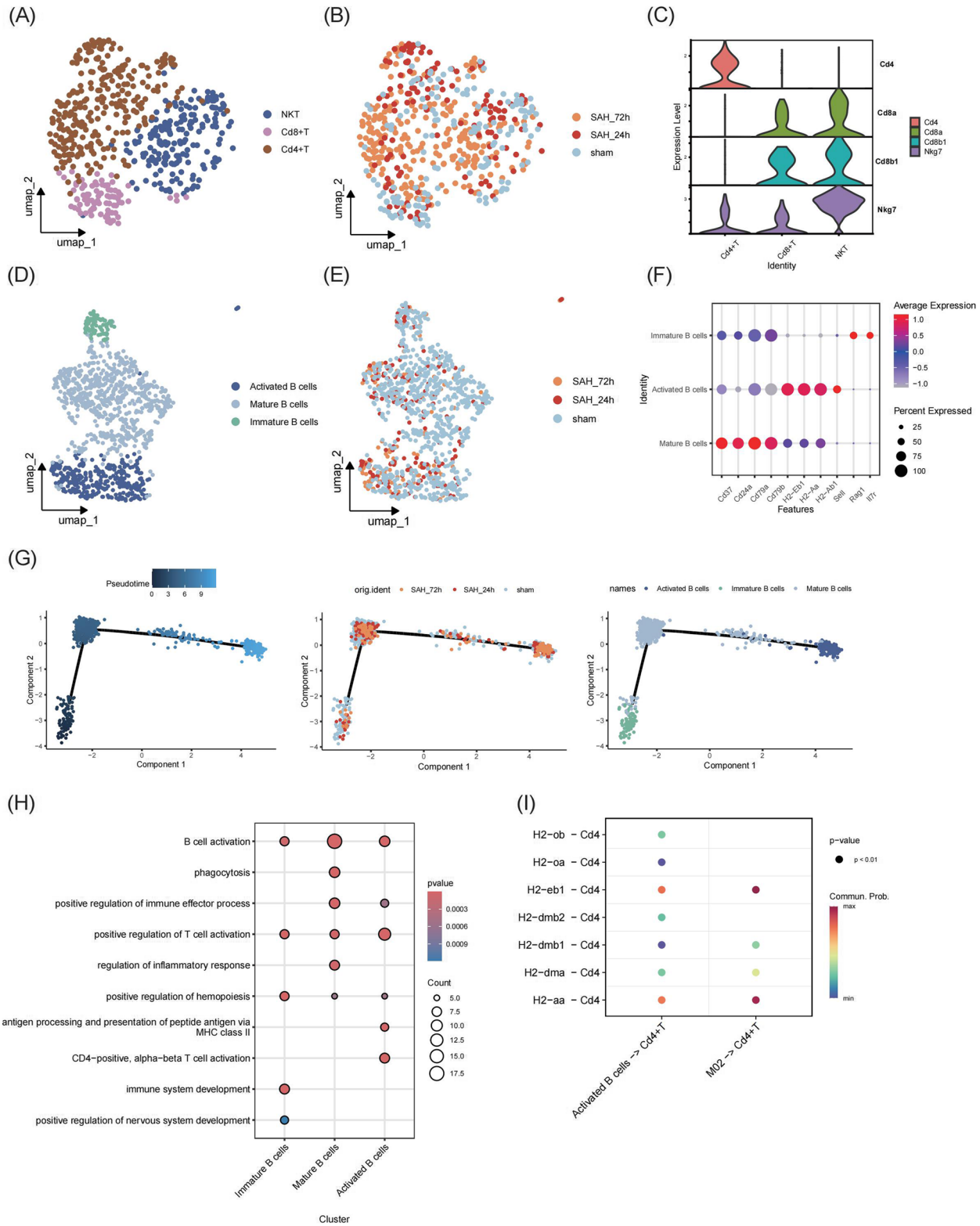

Fig. 5 Transcriptional response of meningeal lymphocytes post-SAH. **A**, **B** UMAP projection of meningeal T cell subclusters colored by clusters (**A**) and samples (**B**). **C** Violin plot showing the expression levels of marker genes in each T cell subpopulation. **D**, **E** UMAP embedding of meningeal B cell subclusters colored by clusters (**D**) and samples (**E**). **F** Dot plot showing the expression levels of marker genes in each B cell subpopulation. **G** Developmental trajectories of meningeal B cell subclusters. **H** GO enrichment analyses of DEGs among the B cell subpopulations. **I** Bubble plot showing the intercellular communication of MHC II signaling pathway at 72 h post-SAH

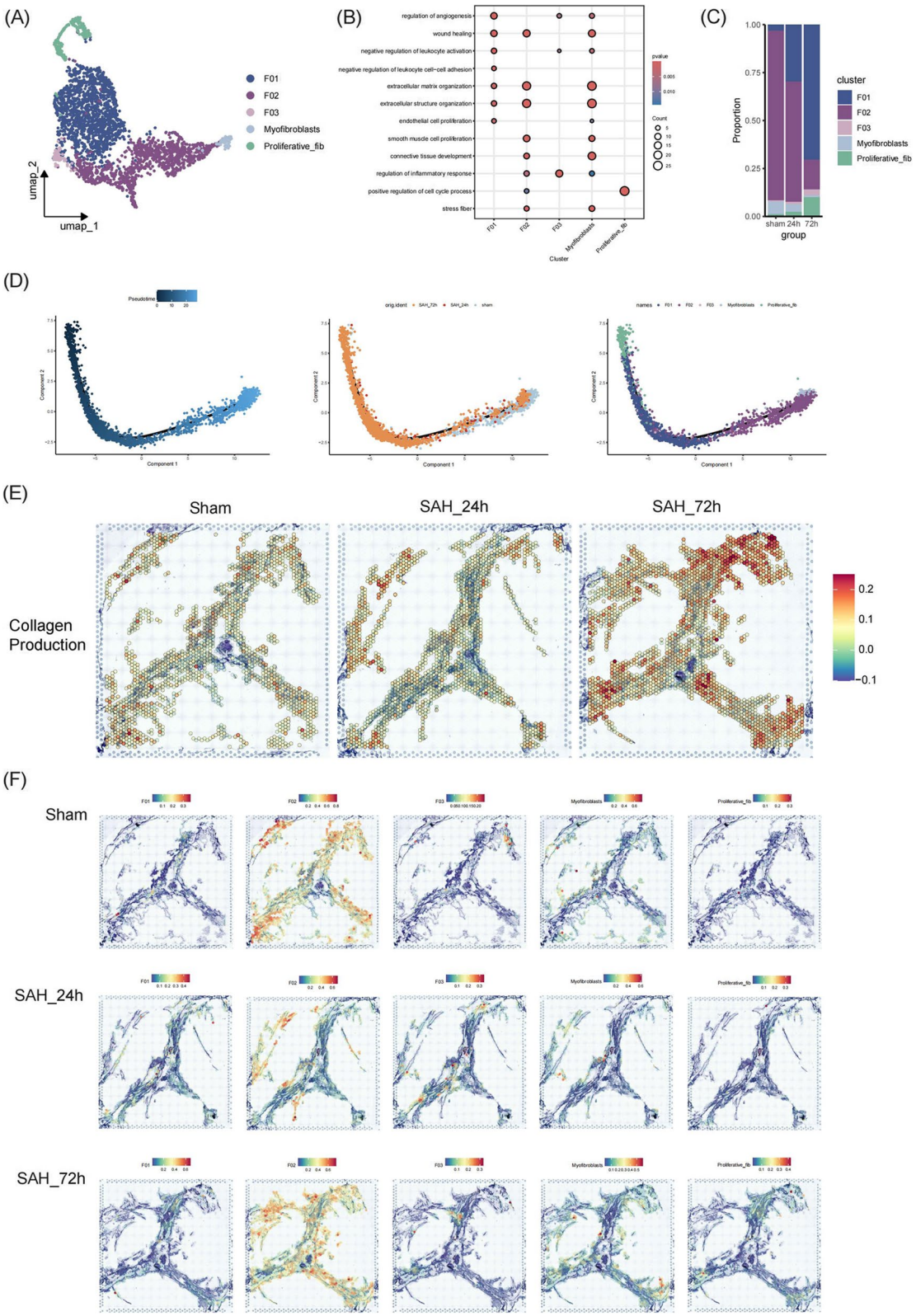

Fig. 6 The phenotype transition of meningeal fibroblasts after SAH. **A** UMAP projection of meningeal fibroblast subclusters colored by clusters. **B** GO enrichment analyses of DEGs among the fibroblast subtypes. **C** Stacked bar plot showing the proportion of meningeal fibroblast subtypes in each group. **D** Developmental trajectories of meningeal fibroblasts subclusters. **E** Projection of collagen production module score for Collagen Biosynthetic Process GO term (GO: 0032964). **F** Predicted spatial localization of meningeal fibroblast subpopulations around mLVs by RCTD

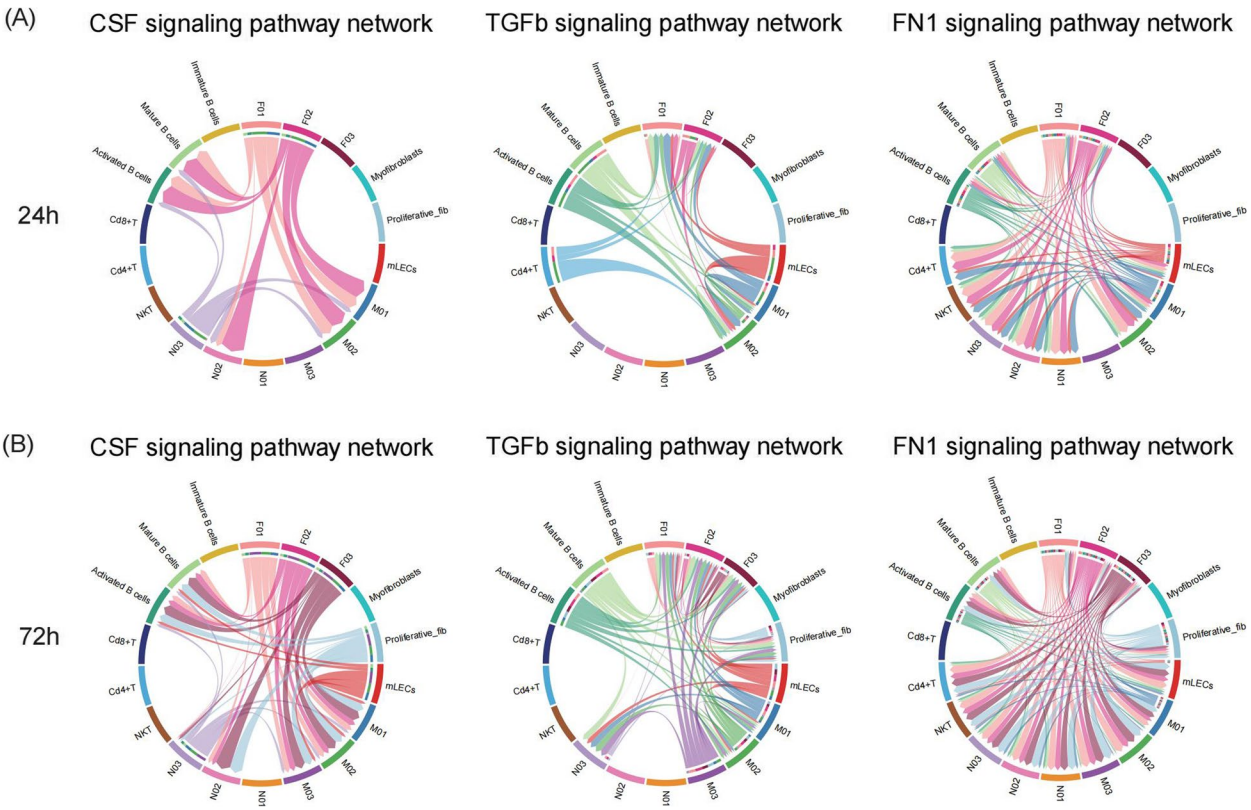

Fig. 7 The immune-fibroblast crosstalk following SAH. **A**, **B** Chord plots of CSF, TGFβ and FN1 signaling network among fibroblasts and immune cells at 24 h (**A**) and 72 h (**B**) post-SAH. Arrows represented signals from the releasing cells to the receptor cells

F01 and proliferative fibroblast subpopulations, are the main source of PGF (Fig. 8A-C).

We administered recombinant protein (VEGF-C/PGF) into the cisterna magna to emulate the acute intrathecal injection treatment in the early phase of SAH (Fig. 8D). The meningeal lymphatic drainage function and neurological outcomes were assessed at 24 h post-SAH. Compared to the Vehicle and VEGF-C groups, acute PGF treatment preserved the Lyve1^{+} vascular density at a higher level (Fig. 8E, F). PGF resulted in better meningeal lymphatic drainage function compared to both Vehicle and VEGF-C (Fig. 8E, G). There was a prominent

(See figure on next page.)

Fig. 8 PGF administration reversed SAH induced meningeal lymphatic dysfunction and neurological deficits in SAH mice. **A** Chord plots of VEGF signaling network among fibroblasts and immune cells at 72 h post-SAH. Arrows represented signals from the releasing cells to the receptor cells. **B** Bubble plot showing the intercellular communication of VEGF signaling pathway at 72 h post-SAH. The releasing cells were fibroblasts and the receptor cells were mLECs. **C** Violin plot showing the expression levels of Pgf gene in each fibroblast subpopulation. **D** Experimental setting: (Left) Mice were induced SAH through a prechiasmatic cistern blood injection and, after 1 h, received an ICM injection of either recombinant VEGF-C/PGF or vehicle. (Right) Mice received a prechiasmatic cistern injection of a mixture of antibodies (IgG/AntiPGF) with autologous blood. **E** Representative image of the mLVs area and beads area in Sham, SAH 24 h + Vehicle, SAH 24 h + VEGF-C and SAH 24 h + PGF group. **F** Quantification of the Lyve1 +/CD31 + vascular density ratio of the mLVs in the different groups ($n = 4$, Kruskal–Wallis test). **G** Measurement of the mean fluorescence intensity of beads in the mLVs in the different groups ($n = 4$, one-way ANOVA). **H** Representative image of the beads at dCLN in the different groups. **I** Quantification of the beads volume at dCLN ($n = 4$, one-way ANOVA, each data point represented unilateral dCLN from one mouse). **J** Neurofunction scores in each group at 24 h post-SAH ($n = 10$, Kruskal–Wallis test for Modified Garcia Score, one-way ANOVA for others). **K** Representative image of the mLVs area and beads area in SAH 72 h + IgG and SAH 72 h + AntiPGF group. **L** Neurofunction scores in each group at 72 h post-SAH ($n = 10$, unpaired two-tailed Student's t-test). **M** Quantification of the Lyve1 +/CD31 + vascular density ratio of the mLVs ($n = 4$, unpaired two-tailed Student's t-test) **N** Measurement of the mean fluorescence intensity of beads in the mLVs in the different groups ($n = 4$, unpaired two-tailed Student's t-test). **O** Quantification of the beads volume at dCLN in the different groups ($n = 4$, unpaired two-tailed Student's t-test). **P** Representative image of the beads at dCLN in the different groups. All data was represented as mean ± SD. *$p < 0.05$, **$p < 0.01$, ***$p < 0.001$, ****$p < 0.0001$, ns represents no statistical difference

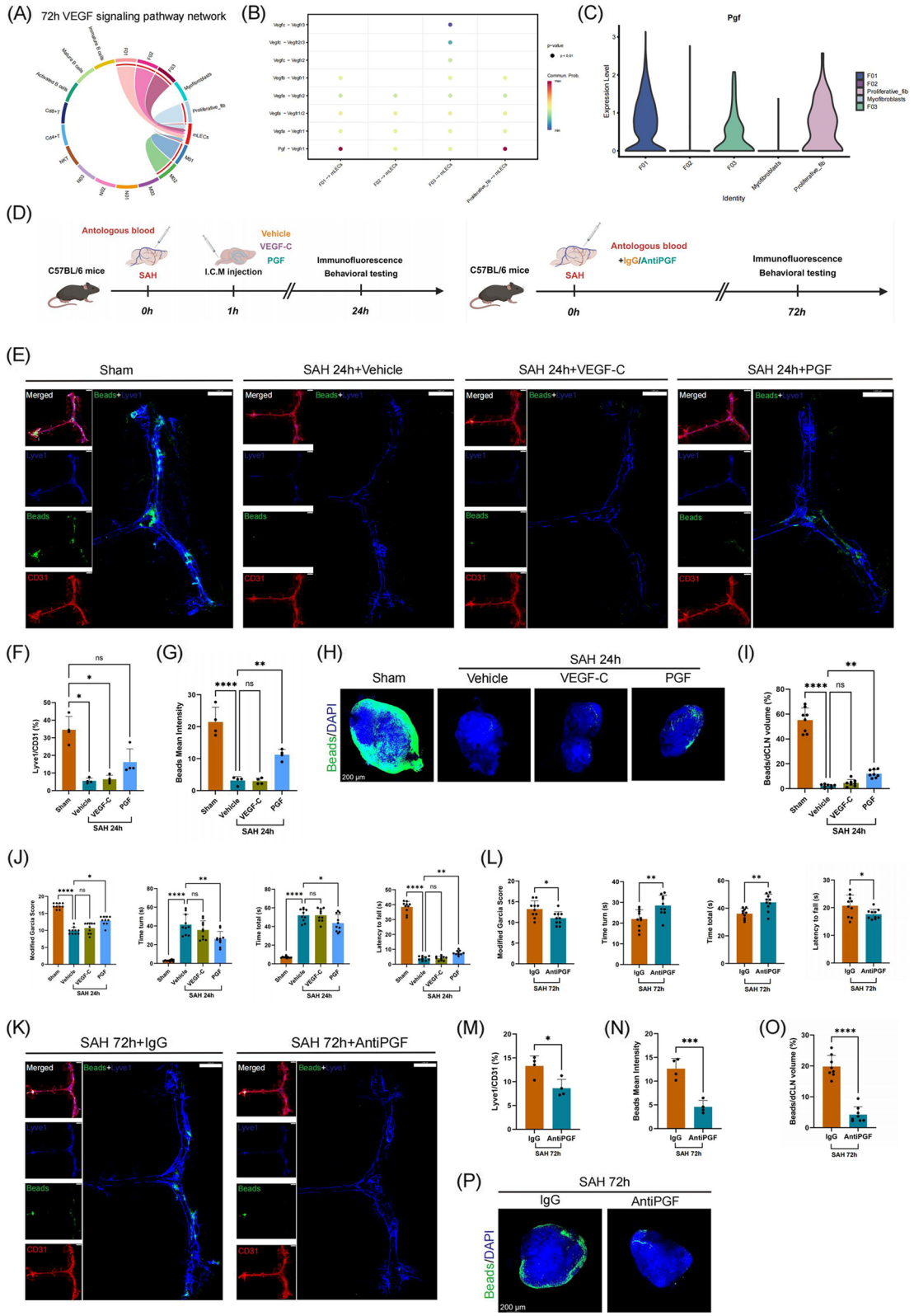

Fig. 8 (See legend on previous page.)

increase in the accumulation of fluorescent beads in dCLNs (Fig. 8H, I). Moreover, the neurological deficits following SAH were alleviated by PGF treatment (Fig. 8J). Next, we used PGF-antibody to further illustrate whether the blockage of PGF would exacerbate the dysfunction of mLVs (Fig. 8D). The results showed that AntiPGF reduced the Lyve1$^+$ area proportion of the mLVs compared to IgG treatment at 72 h post-SAH (Fig. 8K, M). Additionally, the inhibition of PGF aggravated neurological deficits and the dysfunction of meningeal lymphatic system after SAH (Fig. 8K-P).

Discussion

In this study, we systematically analyzed the spatiotemporal changes of meningeal immune cells and fibroblasts following SAH, with a particular focus on immune-fibroblast interactions and their potential roles in regulating meningeal lymphatic drainage. Our findings highlight the critical involvement of myeloid cells and fibroblasts in the acute injury and early repair of meningeal lymphatic drainage function post-SAH. The key discoveries of this study include: (1) Monocyte-derived macrophages early infiltrated the mLVs within 24 h post-SAH, while antigen-presenting macrophages accumulated around the mLVs at 72 h, contributing to T cell activation; (2) A pro-inflammatory neutrophil subset underwent sustained self-recruitment via the CXCL2-CXCR2 axis at 24 h post-SAH, exacerbating meningeal inflammation; (3) By 72 h post-SAH, fibroblast proliferation facilitated tissue remodeling and angiogenesis; (4) Immune-fibroblast crosstalk played a crucial role in shaping the meningeal microenvironment; and (5) Following SAH-induced inflammatory injury, PGF emerged as a potential growth factor that may facilitate the early repair of meningeal lymphatic drainage function.

Macrophages exhibit a dual role in inflammation, neuronal injury and repair after SAH. Previous studies have shown that *Spp1*$^+$ macrophages are associated with inflammation, metabolic reprogramming, and fibrosis in aneurysmal subarachnoid hemorrhage (aSAH), suggesting their involvement in early disease progression [38]. In contrast, *Mrc1*$^+$ macrophages have been reported to alleviate early neuroinflammation and enhance neurological recovery following acute neural injury [39]. Increased *Cd163*$^+$ macrophages in the cerebrospinal fluid of SAH patients correlate with improved prognosis [40]. Similarly, our findings aligned with these observations, revealing that *Spp1*$^+$ monocyte-derived macrophages (M01) rapidly infiltrated the mLVs within 24 h post-SAH. GO enrichment analysis suggested that M01 might be involved in leukocyte migration, activation and acute inflammatory responses. By 72 h post-SAH, the predominant macrophage subsets shifted to M02 (antigen-presenting phenotype, linked to T cell activation) and M03 (homeostatic meningeal macrophages with high Mrc1 and Cd163 expression). This temporal shift suggested a dynamic transformation of macrophages from an inflammatory to a reparative phenotype, with potential implications for the activation of meningeal lymphocytes in the subacute phase as well as meningeal lymphatic system recovery.

Neutrophils are pivotal mediators of tissue injury in SAH. Previous studies have shown that neutrophil extracellular traps (NETs) contribute to neuroinflammation and secondary brain injury post-SAH [41], and that intravascular and perivascular NETs formation exacerbates cerebral vasospasm and delayed cerebral ischemia (DCI) [42, 43]. In addition, NETs formation in the meninges has been implicated in meningeal lymphatic dysfunction via the CX3 CR1 pathway in mouse models of intraventricular hemorrhage (IVH) [44]. Our study further confirmed that neutrophils are the most abundant immune cell type at 24 h post-SAH, with N03 subset localized to inflammatory hotspots around the bilateral transverse sinuses of the mLVs. This coincided with the peak period of acute meningeal lymphatic dysfunction. The N03 subpopulation underwent sustained self-recruitment via CXCL2-CXCR2 signaling. Self-recruitment of neutrophils has been reported in myocarditis, ischemic stroke, and bacterial infection. The CXCL2-CXCR2 ligand-receptor pair is regarded as one of the principal mechanisms facilitating neutrophil self-chemotaxis [31, 32, 45]. Notably, peripheral neutrophils have been reported to lack the self-recruiting subtype under steady-state conditions [31, 32]. Peripheral neutrophils may initially respond to early chemotactic signals released from the damaged tissue and migrate into injured sites. In the acute inflammatory environment, they subsequently transition into a self-recruiting phenotype. The mechanisms underlying this phenotypic shift warrant further investigation, particularly given the complex meningeal microenvironment, where neutrophils originating from both skull bone marrow and peripheral circulation might coexist during acute inflammatory responses. Additionally, given its role in amplifying inflammatory storms, targeting this self-recruitment mechanism may represent a promising therapeutic strategy for reducing acute inflammation in SAH.

Fibroblasts are the predominant stromal cells in the meninges, playing essential roles in CNS development, ECM deposition and vascular remodeling [46]. In response to TBI, fibroblasts secrete ECM components and activate immune pathways to facilitate wound healing [36]. Furthermore, meningeal fibroblasts have been demonstrated to regulate the proliferation of meningeal vessel endothelial cells [47]. In this study, we identified

a marked expansion of fibroblasts at 72 h post-SAH, particularly the F01 subpopulation, which was highly enriched in genes associated with angiogenesis, wound healing, and immune regulation. Integrating the results from scRNA-seq and ST-seq, we hypothesized that meningeal immature fibroblasts (F01 subpopulation and proliferative fibroblasts) might grow and develop within 72 h post-SAH. These newly formed fibroblast subtypes might play a role in the recovery of the drainage function of mLVs following acute inflammation. Spatially, F02 and myofibroblast subsets were localized around the mLVs, expressing genes involved in ECM production and connective tissue development. The spatial module score associated with collagen production was significantly elevated at 72 h post-SAH, which suggested that fibroblast activation and proliferation might induce ECM remodeling around mLVs in the subacute phase of SAH. Fibroblasts may contribute to early meningeal lymphatic repair by modulating ECM composition and promoting vascular remodeling. However, excessive fibroblast activation could lead to meningeal fibrosis, a potential long-term complication that could impair meningeal lymphatic drainage function and warranted further investigation.

In various diseases, immune cells infiltrate tissues and undergo subtype transformation. The interactions between fibroblasts and immune cells are critical in disease progression, particularly in tissue repair, inflammation resolution, and fibrosis [4, 36, 48–50]. Our analysis revealed that meningeal fibroblasts interacted with macrophages via CSF1-CSF1R signaling pathway, which has been shown to promote monocyte-derived macrophage differentiation into anti-inflammatory and reparative phenotypes, especially in the ischemic and hypoxic microenvironment [48, 51, 52]. This suggests that fibroblasts may drive macrophage polarization from an inflammatory (M01) to a reparative (M02) phenotype post-SAH. Additionally, fibroblasts interacted with neutrophils, macrophages, and T cells via fibronectin (FN1 signaling), a key ECM protein involved in cell adhesion, migration, and tissue remodeling [53, 54]. FN1 was reported to regulate the immune response of myeloid cells [55]. Meanwhile, macrophage derived TGFβ1 signaling to fibroblasts (via ACVR1/TGFβR1) might drive fibroblast activation and collagen synthesis, potentially contributing to the fibroblast expansion observed at 72 h post-SAH [52]. The TGFβ signals were reported to participate in the fibrosis, matrix remodeling and angiogenesis [49].

The VEGF family is essential for the development of vascular and lymphatic networks [56]. VEGF-C and VEGF-D are recognized as the principal growth factors regulating lymphatic development, primarily signal via VEGFR3 [56]. VEGF-C-VEGFR3 ligand-receptor pair plays a pivotal role in the development of the central lymphatic system [37]. Pretreatment with VEGF-C can stimulate the growth of mLVs and enhance drainage efficiency [11, 22]. Inhibition of VEGF-C leads to limited development and growth of mLVs, impairing drainage function, whereas inhibition of VEGF-D does not produce similar adverse effects [37]. Compared with VEGF-C, VEGF-D exerts a significantly weaker regulatory effect on the central lymphatic system [37]. VEGF-C is regarded as the critical growth factor for maintaining the normal structure and drainage function of the meningeal lymphatic system under physiological conditions [37, 57]. However, early VEGF-C treatment has failed to improve the drainage function of the meningeal lymphatic system following ischemic stroke, raising concerns about its reparative potential in acute inflammation settings [22]. Acute inflammatory response may lead to the reduced expression of VEGFR3 on mLECs, thereby limiting the efficacy of VEGF-C during the acute phase [22, 58]. Communication analysis suggested that PGF was the strongest ligand in the VEGF signaling network received by mLECs at 72 h post-SAH. We further pinpointed F01 fibroblasts as the primary source of PGF, suggesting that fibroblasts may contribute to early repair of mLVs via PGF-VEGFR1 signaling following SAH. Our findings suggested that PGF, rather than VEGF-C, play a more critical role in the early repair of damaged mLVs post-SAH. Exogenous PGF preserved the $Lyve1^{+}$ vascular density in the mLVs, enhanced drainage efficiency and improved neurological outcomes at 24 h post-SAH. Conversely, PGF inhibition would impair the recovery of mLVs at 72 h. These findings supported PGF as a promising therapeutic target for enhancing meningeal lymphatic function and mitigating secondary brain injury after SAH. Notably, PGF has been shown to promote pathological vessel formation and regeneration in the inflammatory environment [59–61]. PGF may participate in the survival and growth of a specific mLEC subpopulation, thereby maintaining structural integrity and drainage function of mLVs in the acute phase following SAH. However, the long-term efficacy of PGF remains uncertain. Chronic PGF exposure may paradoxically induce pathological lymphangiogenesis, potentially contributing to persistent drainage inefficiency during the chronic phase—a critical consideration warranting further investigation.

Despite its strengths, this study has several limitations: First, animal models do not fully recapitulate the complex pathophysiology of human SAH. Second, scRNA-seq and ST-seq provide only static snapshots, limiting our ability to capture real-time cellular dynamics in the meningeal microenvironment. Third, bioinformatics-based cell subpopulation analysis requires validation with cytometry and functional assays to fully elucidate differentiation

pathways. Fourth, the mechanistic details of PGF-mediated meningeal lymphatic repair and its downstream effectors remain to be explored.

Conclusion

Our study, utilizing single-cell resolution analysis, uncovered a dynamic transition in the meningeal microenvironment with the first 72 h post-SAH, shifting from a "myeloid cell-mediated acute inflammatory response" to an "immune-fibroblast interaction-mediated tissue remodeling process". This transformation was closely associated with the early drainage dysfunction and subsequent recovery of meningeal lymphatic drainage. Targeting the phenotype transition of meningeal immune cells and fibroblasts may offer a promising therapeutic strategy to enhance meningeal lymphatic function and mitigate secondary brain injury following SAH.

Abbreviations

CNS	Central nervous system
mLVs	Meningeal lymphatic vessels
SAH	Subarachnoid hemorrhage
ICH	Intracerebral hemorrhage
scRNA-seq	Single-cell RNA sequencing
ST-seq	Spatial transcriptomics
dCLNs	Deep cervical lymph nodes
ICM	Intra-cisterna magna
UMAP	Uniform manifold approximation and projection
DEGs	Differentially expressed genes
GSEA	Gene set enrichment analyses
GO	Gene ontology
KEGG	Kyoto encyclopedia of genes and genomes
mLECs	Meningeal lymphatic endothelial cells
RCTD	Robust cell type decomposition
SD	Standard deviation
ANOVA	One-way analysis of variance
APCs	Antigen-presenting cells
ECM	Extracellular matrix
CCL	C-C motif chemokine ligand
CXCL	C-X-C motif chemokine ligand
CSF	Colony stimulating factor
TGFβ	Transforming growth factor beta
FN1	Fibronectin 1
PGF	Placental growth factor
VEGF-C	Vascular endothelial growth factor C
VEGFR1	Vascular endothelial growth factor receptor 1
VEGFR3	Vascular endothelial growth factor receptor 3
aSAH	Aneurysmal subarachnoid hemorrhage
NETs	Neutrophil extracellular traps
DCI	Delayed cerebral ischemia
IVH	Intraventricular hemorrhage

Supplementary Information

The online version contains supplementary material available at https://doi.org/10.1186/s12974-025-03460-0.

Supplementary Material 1.

Supplementary Material 2.

Supplementary Material 3.

Supplementary Material 4.

Supplementary Material 5.

Supplementary Material 6.

Supplementary Material 7.

Supplementary Material 8.

Supplementary Material 9.

Acknowledgements

We thank the Second Affiliated Hospital of Zhejiang University School of Medicine for supporting this work. The authors acknowledge that some figures were created using BioRender (https://biorender.com/).

Authors' contributions

BRZ, CML and ML contributed equally to this work. XYW, SC, YJF and JMZ designed this study. XYW, SC, YJF, JMZ and ZW supervised this study. BRZ, SXT, TTZ, YBL, HCZ performed all experiments. BRZ, CML and JRC provided technical support for scRNA-Seq and ST-seq data analysis. BRZ, CML and ML contributed to statistical analysis. BRZ, CML and ML wrote the original manuscript. XYW, SC, YJF, JMZ and ZW critically revised manuscript and polish the language. All authors helped to conduct this study, read, and approved the final manuscript.

Funding

This study was supported by Noncommunicable Chronic Diseases-National Science and Technology Major Project (Grant 2023ZD0505100 to Sheng Chen), the National Natural Science Foundation of China (Grant 82371300 to Sheng Chen), the National Natural Science Foundation of China (Grant 82201430 to Yuanjian Fang), the Natural Science Foundation of Zhejiang Province (Grant LY23H090014 to Sheng Chen), the Medical Health Science and Technology Project of Zhejiang Provincial Health Commission (Grant WKJ-ZJ-2427 to Sheng Chen), the Natural Science Foundation of Zhejiang Province (Grant LTGD23 C040010 to Zhen Wang).

Data availability

The datasets used and/or analyzed during the current study are available from the corresponding author on reasonable request.

Declarations

Ethics approval and consent to participate

This study was approved by the Institutional Ethics Committee of the Second Affiliated Hospital, Zhejiang University School of Medicine (Approval No. 2024–220). All animal procedures were approved by the Animal Use and Care Committee of the Second Affiliated Hospital of Zhejiang University School of Medicine, Hangzhou, China.

Consent for publication

All authors have approved the manuscript for publication.

Competing interests

The authors declare no competing interests.

Author details

[1]Department of Neurosurgery, The Second Affiliated Hospital, School of Medicine, Zhejiang University, Hangzhou 310009, China. [2]Key Laboratory of Precise Treatment and Clinical Translational Research of Neurological Diseases, Hangzhou 310009, Zhejiang, China. [3]State Key Laboratory of Transvascular Implantation Devices, Hangzhou 310009, China. [4]Zhejiang University School of Medicine, Hangzhou 310058, China. [5]Department of Neurosurgery, Lishui Central Hospital, The Fifth Affiliated Hospital of Wenzhou Medical University, Lishui 323000, China.

Received: 26 March 2025 Accepted: 2 May 2025
Published online: 16 May 2025

References

1. Betsholtz C, Engelhardt B, Koh GY, McDonald DM, Proulx ST, Siegenthaler J. Advances and controversies in meningeal biology. Nat Neurosci. 2024;27:2056–72.

2. Wang X, Zhang A, Yu Q, Wang Z, Wang J, Xu P, et al. Single-Cell RNA Sequencing and Spatial Transcriptomics Reveal Pathogenesis of Meningeal Lymphatic Dysfunction after Experimental Subarachnoid Hemorrhage. Adv Sci (Weinh). 2023;10: e2301428.
3. Xue X, Wu X, Fan Y, Han S, Zhang H, Sun Y, et al. Heterogeneous fibroblasts contribute to fibrotic scar formation after spinal cord injury in mice and monkeys. Nat Commun. 2024;15:6321.
4. Amrute JM, Luo X, Penna V, Yang S, Yamawaki T, Hayat S, et al. Targeting immune-fibroblast cell communication in heart failure. Nature. 2024;635:423–33.
5. Da Mesquita S, Papadopoulos Z, Dykstra T, Brase L, Farias FG, Wall M, et al. Meningeal lymphatics affect microglia responses and anti-Abeta immunotherapy. Nature. 2021;593:255–60.
6. Zou W, Pu T, Feng W, Lu M, Zheng Y, Du R, et al. Blocking meningeal lymphatic drainage aggravates Parkinson's disease-like pathology in mice overexpressing mutated alpha-synuclein. Transl Neurodegener. 2019;8:7.
7. Chen J, Wang L, Xu H, Wang Y, Liang Q. The lymphatic drainage system of the CNS plays a role in lymphatic drainage, immunity, and neuroinflammation in stroke. J Leukoc Biol. 2021;110:283–91.
8. Liao J, Zhang M, Shi Z, Lu H, Wang L, Fan W, et al. Improving the Function of Meningeal Lymphatic Vessels to Promote Brain Edema Absorption after Traumatic Brain Injury. J Neurotrauma. 2023;40:383–94.
9. Tsai HH, Hsieh YC, Lin JS, Kuo ZT, Ho CY, Chen CH, et al. Functional Investigation of Meningeal Lymphatic System in Experimental Intracerebral Hemorrhage. Stroke. 2022;53:987–98.
10. Chen J, Wang L, Xu H, Xing L, Zhuang Z, Zheng Y, et al. Meningeal lymphatics clear erythrocytes that arise from subarachnoid hemorrhage. Nat Commun. 2020;11:3159.
11. Gao D, Zou B, Zhu K, Bi S, Zhang W, Yang X, et al. Enhancing Th17 cells drainage through meningeal lymphatic vessels alleviate neuroinflammation after subarachnoid hemorrhage. J Neuroinflammation. 2024;21:269.
12. Ding PF, Xing CJ, Gao YY, Hang CH, Zhuang Z, Li W. Analysis and prediction of subarachnoid hemorrhage burden in global, China, and Japan. BMC Public Health. 2025;25:27.
13. Collaborators GBDSRF. Global, regional, and national burden of stroke and its risk factors, 1990–2021: a systematic analysis for the Global Burden of Disease Study 2021. Lancet Neurol 2024, 23: 973–1003.
14. Akeret K, Buzzi RM, Schaer CA, Thomson BR, Vallelian F, Wang S, et al. Cerebrospinal fluid hemoglobin drives subarachnoid hemorrhage-related secondary brain injury. J Cereb Blood Flow Metab. 2021;41:3000–15.
15. Fang Y, Wang X, Lu J, Shi H, Huang L, Shao A, et al. Inhibition of caspase-1-mediated inflammasome activation reduced blood coagulation in cerebrospinal fluid after subarachnoid haemorrhage. EBioMedicine. 2022;76: 103843.
16. Fang Y, Liu Y, Chen L, Wang J, Zhang J, Zhang H, et al. Cerebrospinal fluid markers of neuroinflammation and coagulation in severe cerebral edema and chronic hydrocephalus after subarachnoid hemorrhage: a prospective study. J Neuroinflammation. 2024;21:237.
17. Fang Y, Shao Y, Lu J, Dong X, Zhao X, Zhang J, et al. The effectiveness of lumbar cerebrospinal fluid drainage in aneurysmal subarachnoid hemorrhage with different bleeding amounts. Neurosurg Rev. 2020;43:739–47.
18. Eide PK, Undseth RM, Pripp A, Lashkarivand A, Nedregaard B, Sletteberg R, et al. Impact of Subarachnoid Hemorrhage on Human Glymphatic Function: A Time-Evolution Magnetic Resonance Imaging Study. Stroke 2025.
19. Pu T, Zou W, Feng W, Zhang Y, Wang L, Wang H, et al. Persistent Malfunction of Glymphatic and Meningeal Lymphatic Drainage in a Mouse Model of Subarachnoid Hemorrhage. Exp Neurobiol. 2019;28:104–18.
20. Sabri M, Jeon H, Ai J, Tariq A, Shang X, Chen G, et al. Anterior circulation mouse model of subarachnoid hemorrhage. Brain Res. 2009;1295:179–85.
21. Bolte AC, Dutta AB, Hurt ME, Smirnov I, Kovacs MA, McKee CA, et al. Meningeal lymphatic dysfunction exacerbates traumatic brain injury pathogenesis. Nat Commun. 2020;11:4524.
22. Boisserand LSB, Geraldo LH, Bouchart J, El Kamouh MR, Lee S, Sanganahalli BG, et al. VEGF-C prophylaxis favors lymphatic drainage and modulates neuroinflammation in a stroke model. J Exp Med 2024, 221.
23. Chen H, Xu C, Zeng H, Zhang Z, Wang N, Guo Y, et al. Ly6C-high monocytes alleviate brain injury in experimental subarachnoid hemorrhage in mice. J Neuroinflammation. 2023;20:270.
24. Hao Y, Stuart T, Kowalski MH, Choudhary S, Hoffman P, Hartman A, et al. Dictionary learning for integrative, multimodal and scalable single-cell analysis. Nat Biotechnol. 2024;42:293–304.
25. Hu C, Li T, Xu Y, Zhang X, Li F, Bai J, et al. CellMarker 2.0: an updated database of manually curated cell markers in human/mouse and web tools based on scRNA-seq data. Nucleic Acids Res 2023, 51: D870-D876.
26. Franzen O, Gan LM, Bjorkegren JLM. PanglaoDB: a web server for exploration of mouse and human single-cell RNA sequencing data. Database (Oxford) 2019, 2019.
27. Wu T, Hu E, Xu S, Chen M, Guo P, Dai Z, et al. clusterProfiler 4.0: A universal enrichment tool for interpreting omics data. Innovation (Camb) 2021, 2: 100141.
28. Castanza AS, Recla JM, Eby D, Thorvaldsdottir H, Bult CJ, Mesirov JP. Extending support for mouse data in the Molecular Signatures Database (MSigDB). Nat Methods. 2023;20:1619–20.
29. Qiu X, Mao Q, Tang Y, Wang L, Chawla R, Pliner HA, et al. Reversed graph embedding resolves complex single-cell trajectories. Nat Methods. 2017;14:979–82.
30. Jin S, Guerrero-Juarez CF, Zhang L, Chang I, Ramos R, Kuan CH, et al. Inference and analysis of cell-cell communication using Cell Chat. Nat Commun. 2021;12:1088.
31. Li H, Zhang M, Zhao Q, Zhao W, Zhuang Y, Wang J, et al. Self-recruited neutrophils trigger over-activated innate immune response and phenotypic change of cardiomyocytes in fulminant viral myocarditis. Cell Discov. 2023;9:103.
32. Gu Y, Zhang X, Li H, Wang R, Jin C, Wang J, et al. Novel subsets of peripheral immune cells associated with promoting stroke recovery in mice. CNS Neurosci Ther. 2024;30: e14518.
33. Marin-Rodero M, Cintado E, Walker AJ, Jayewickreme T, Pinho-Ribeiro FA, Richardson Q, et al. The meninges host a distinct compartment of regulatory T cells that preserves brain homeostasis. Sci Immunol 2025: eadu2910.
34. Fitzpatrick Z, Ghabdan Zanluqui N, Rosenblum JS, Tuong ZK, Lee CYC, Chandrashekhar V, et al. Venous-plexus-associated lymphoid hubs support meningeal humoral immunity. Nature. 2024;628:612–9.
35. Shen J, Bian N, Zhao L, Wei J. The role of T-lymphocytes in central nervous system diseases. Brain Res Bull. 2024;209: 110904.
36. Bolte AC, Shapiro DA, Dutta AB, Ma WF, Bruch KR, Kovacs MA, et al. The meningeal transcriptional response to traumatic brain injury and aging. Elife 2023, 12.
37. Antila S, Karaman S, Nurmi H, Airavaara M, Voutilainen MH, Mathivet T, et al. Development and plasticity of meningeal lymphatic vessels. J Exp Med. 2017;214:3645–67.
38. Jie H, Wang B, Zhang J, Wang X, Song X, Yang F, et al. Uncovering SPP1(+) Macrophage, Neutrophils and Their Related Diagnostic Biomarkers in Intracranial Aneurysm and Subarachnoid Hemorrhage. J Inflamm Res. 2024;17:8569–87.
39. Yang S, Yu B, Zhang Q, Zhang Y, Fu L, Zhou B, et al. Amantadine modulates novel macrophage phenotypes to enhance neural repair following spinal cord injury. J Transl Med. 2025;23:60.
40. Thomas AJ, Ogilvy CS, Griessenauer CJ, Hanafy KA. Macrophage CD163 expression in cerebrospinal fluid: association with subarachnoid hemorrhage outcome. J Neurosurg. 2019;131:47–53.
41. Zeng H, Fu X, Cai J, Sun C, Yu M, Peng Y, et al. Neutrophil Extracellular Traps may be a Potential Target for Treating Early Brain Injury in Subarachnoid Hemorrhage. Transl Stroke Res. 2022;13:112–31.
42. Zeineddine HA, Hong SH, Peesh P, Dienel A, Torres K, Thankamani Pandit P, et al. Neutrophils and Neutrophil Extracellular Traps Cause Vascular Occlusion and Delayed Cerebral Ischemia After Subarachnoid Hemorrhage in Mice. Arterioscler Thromb Vasc Biol. 2024;44:635–52.
43. Nakagawa R, Itokazu T, Shibuya N, Kishima H, Yamashita T. Perivascular Neutrophil Extracellular Traps Exacerbate Microvasospasm After Experimental Subarachnoid Hemorrhage. Stroke. 2024;55:2872–81.
44. Zhang Q, Chen Y, Li Y, Feng Z, Liang L, Hao X, et al. Neutrophil extracellular trap-mediated impairment of meningeal lymphatic drainage exacerbates secondary hydrocephalus after intraventricular hemorrhage. Theranostics. 2024;14:1909–38.
45. Kienle K, Glaser KM, Eickhoff S, Mihlan M, Knopper K, Reategui E, et al. Neutrophils self-limit swarming to contain bacterial growth in vivo. Science 2021, 372.
46. DeSisto J, O'Rourke R, Jones HE, Pawlikowski B, Malek AD, Bonney S, et al. Single-Cell Transcriptomic Analyses of the Developing Meninges Reveal Meningeal Fibroblast Diversity and Function. Dev Cell. 2020;54(43–59): e44.

47. Ai D, Ming T, Li X, Wang S, Bi Z, Zuo J, et al. Transcriptomic Profiling Unveils EDN3(+) Meningeal Fibroblasts as Key Players in Sturge-Weber Syndrome Pathogenesis. Adv Sci (Weinh) 2025: e2408888.
48. Kapanadze T, Gamrekelashvili J, Sablotny S, Kijas D, Haller H, Schmidt-Ott K, et al. CSF-1 and Notch signaling cooperate in macrophage instruction and tissue repair during peripheral limb ischemia. Front Immunol. 2023;14:1240327.
49. Venugopal H, Hanna A, Humeres C, Frangogiannis NG. Properties and Functions of Fibroblasts and Myofibroblasts in Myocardial Infarction. Cells 2022, 11.
50. Wang Y, Shen Z, Mo S, Zhang H, Chen J, Zhu C, et al. Crosstalk among proximal tubular cells, macrophages, and fibroblasts in acute kidney injury: single-cell profiling from the perspective of ferroptosis. Hum Cell. 2024;37:1039–55.
51. Sehgal A, Irvine KM, Hume DA. Functions of macrophage colony-stimulating factor (CSF1) in development, homeostasis, and tissue repair. Semin Immunol. 2021;54: 101509.
52. Buechler MB, Fu W, Turley SJ. Fibroblast-macrophage reciprocal interactions in health, fibrosis, and cancer. Immunity. 2021;54:903–15.
53. Huet-Calderwood C, Rivera-Molina FE, Toomre DK, Calderwood DA. Fibroblasts secrete fibronectin under lamellipodia in a microtubule- and myosin II-dependent fashion. J Cell Biol 2023, 222.
54. Liu X, Dai K, Zhang X, Huang G, Lynn H, Rabata A, et al. Multiple Fibroblast Subtypes Contribute to Matrix Deposition in Pulmonary Fibrosis. Am J Respir Cell Mol Biol. 2023;69:45–56.
55. Peng Z, Ren Z, Tong Z, Zhu Y, Zhu Y, Hu K. Interactions between MFAP5 + fibroblasts and tumor-infiltrating myeloid cells shape the malignant microenvironment of colorectal cancer. J Transl Med. 2023;21:405.
56. Secker GA, Harvey NL. Regulation of VEGFR Signalling in Lymphatic Vascular Development and Disease: An Update. Int J Mol Sci 2021, 22.
57. Louveau A, Herz J, Alme MN, Salvador AF, Dong MQ, Viar KE, et al. CNS lymphatic drainage and neuroinflammation are regulated by meningeal lymphatic vasculature. Nat Neurosci. 2018;21:1380–91.
58. Yuan J, Liu X, Nie M, Chen Y, Liu M, Huang J, et al. Inactivation of ERK1/2 signaling mediates dysfunction of basal meningeal lymphatic vessels in experimental subdural hematoma. Theranostics. 2024;14:304–23.
59. Zhao Y, Lei Y, Ning H, Zhang Y, Chen G, Wang C, et al. PGF(2alpha) facilitates pathological retinal angiogenesis by modulating endothelial FOS-driven ELR(+) CXC chemokine expression. EMBO Mol Med. 2023;15: e16373.
60. Zhou Y, Tabib T, Huang M, Yuan K, Kim Y, Morse C, et al. Molecular Changes Implicate Angiogenesis and Arterial Remodeling in Systemic Sclerosis-Associated and Idiopathic Pulmonary Hypertension. Arterioscler Thromb Vasc Biol. 2024;44:e210–25.
61. Unterleuthner D, Neuhold P, Schwarz K, Janker L, Neuditschko B, Nivarthi H, et al. Cancer-associated fibroblast-derived WNT2 increases tumor angiogenesis in colon cancer. Angiogenesis. 2020;23:159–77.

Publisher's Note

Springer Nature remains neutral with regard to jurisdictional claims in published maps and institutional affiliations.